Exploring the Water-Binding Pocket of the Type II Dehydroquinase Enzyme in the Structure-Based Design of Inhibitors

*Beatriz Blanco,[1‡] Antía Sedes,[1‡] Antonio Peón,[1] José M. Otero,[2] Mark J. van Raaij,[3] Paul Thompson,[4] Alastair R. Hawkins,[4] and Concepción González-Bello[1]**

[1]Centro Singular de Investigación en Química Biológica y Materiales Moleculares (CIQUS), Universidad de Santiago de Compostela, 15782 Santiago de Compostela, Spain.

[2]Departamento de Bioquímica y Biología Molecular, Centro Singular de Investigación en Química Biológica y Materiales Moleculares (CIQUS), Universidad de Santiago de Compostela, 15782 Santiago de Compostela, Spain.

[3]Departamento de Estructura de Macromoléculas, Centro Nacional de Biotecnología (CSIC), Campus Cantoblanco, 28049 Madrid, Spain.

[4]Institute of Cell and Molecular Biosciences, Medical School, University of Newcastle upon Tyne, Newcastle upon Tyne NE2 4HH, UK.

CORRESPONDING AUTHOR ADDRESS. Dr. Concepción González-Bello. Centro Singular de Investigación en Química Biológica y Materiales Moleculares (CIQUS), Universidad de Santiago de Compostela, calle Jenaro de la Fuente s/n, 15782 Santiago de Compostela, Spain.

ABSTRACT. Structural and computational studies to explore the WAT1 binding pocket in the structure-based design of inhibitors against the type II dehydroquinase (DHQ2) enzyme are reported. The crystal structures of DHQ2 from *M. tuberculosis* in complex with four of the reported compounds are described. The electrostatic interaction observed between the guanidinium group of the essential arginine and the carboxylate group of one of the inhibitors in the reported crystal structures supports the recently suggested role of this arginine as the residue that triggers the release of the product from the active site. The results of the structural and molecular dynamics simulation studies revealed that the inhibitory potency is favored by promoting interactions with WAT1 and the residues located within this pocket and, more importantly, by avoiding situations where the ligands occupy the WAT1 binding pocket. The new insights can be used to advantage in the structure-based design of inhibitors.

INTRODUCTION

The increasing development and spread of resistance to current antibiotics has made infectious diseases the second most common cause of death worldwide.[1] Despite this alarming trend, only two new classes of antibiotics have been brought to the market in the last three decades and there are only a few antibacterial agents under development to face the challenge of multidrug resistance.[2-5] Hence, there is a great deal of interest in the development of alternative therapies, including new strategies for the treatment of infections that are resistant to current antibiotics, in particular drugs with new mechanisms of action to combat the growth of antibiotic-resistant bacteria.[6] One strategy to combat bacterial infections is based on the disruption of the growth cycle by preventing the synthesis and assembly of key components of bacterial processes.[7-8] Many drugs that are highly successful in human clinical use are mimetics of the substrate or intermediates of key enzymatic reactions. For instance, sulfonamide-based drugs are analogs of *p*-aminobenzoate, the natural substrate of dihydropteroate synthase, an essential enzyme in the folic acid biosynthesis pathway. During the past few years, a great deal of effort has been focused on the inhibition of the enzymes involved in the shikimic acid pathway, in which chorismic acid is synthesized. These enzymes are recognized to be attractive targets for the development of new antibacterial agents because they are essential in important pathogenic bacteria but are

absent in mammals.[9] Special attention has been paid to the inhibition of the third enzyme of the pathway, namely type II dehydroquinase (3-dehydroquinate dehydratase, EC 4.2.1.10, DHQ2), which is one of the two known DHQ enzymes. DHQ2 is essential in *Mycobacterium tuberculosis* (*aroD* gene, *Mt*-DHQ2),[10] which is responsible for causing tuberculosis, and *Helicobacter pylori* (*aroD*/*aroQ* gene, *Hp*-DHQ2),[10] which is the causative agent of gastric and duodenal ulcers and has been classified as a type I carcinogen.

DHQ2 catalyzes the reversible dehydration of 3-dehydroquinic acid (**1**) to form 3-dehydroshikimic acid (**2**). The *anti* elimination of water involves the loss of the more acidic pro-*S* hydrogen from C2 of **1** (Scheme 1). After substrate binding, a flexible loop forms a lid that closes the active site. Three residues, an arginine (Arg17/Arg19 in *Hp*-DHQ2 and *Mt*-DHQ2, respectively), a tyrosine (Tyr22/Tyr24 in *Hp*-DHQ2 and *Mt*-DHQ2, respectively) and an aspartate (Asp89*/Asp88* in *Hp*-DHQ2 and *Mt*-DHQ2, respectively) from the neighboring enzyme subunit (residues from this subunit will be marked with an asterisk), were identified by chemical modification and site-directed mutagenesis studies as essential for enzyme activity.[11-13] The elimination proceeds by a stepwise E_1CB mechanism that involves an enolate intermediate **3**.[14,13] The reaction is initiated by the essential Asp89*/Asp88* (Figure 1A). This residue deprotonates the essential Tyr22/Tyr24, which is located in the loop, to afford the catalytic tyrosinate, which in turn triggers the enzymatic process.[13] For the *Hp*-DHQ2 enzyme, this reaction takes place with the assistance of a water molecule, while for *Mt*-DHQ2, the tyrosine is directly deprotonated by the aspartate residue.[13] The guanidinium group of Arg17/Arg19 must be close to the essential tyrosine side chain for catalysis because, in this arrangement, it controls the appropriate orientation of the tyrosine, which is roughly perpendicular to the cyclohexane ring of the natural substrate, through a cation-π interaction and contributes to decreasing the pKa of the phenol group.[15] The tyrosinate removes the axial hydrogen from C2 of **1** to give an enolate intermediate **3** (Figure 1B), which is stabilized by the positively charged side chain of the essential Arg17/Arg19 and by a hydrogen bond between the neutral aspartate Asp89*/Asp88* and a conserved water molecule (henceforth WAT1). The final step is the acid-catalyzed elimination of the C1 hydroxyl group – a reaction mediated by the conserved histidine His102/His101 (in *Hp*-DHQ2 and *Mt*-DHQ2, respectively) acting as a proton donor.

The presence of WAT1 in many crystal structures and its role in the enzymatic mechanism has been widely discussed. This water molecule interacts through hydrogen bonding with a conserved asparagine (Asn10/Asn12 in *Hp*-DHQ2and *Mt*-DHQ2, respectively), the carbonyl group of a conserved proline (Pro9/Pro11 in *Hp*-DHQ2 and *Mt*-DHQ2, respectively), and the main-chain amide of a glycine or an alanine (Ala79/Gly78 in *Hp*-DHQ2 and *Mt*-DHQ2, respectively). Initially, it was proposed that this water molecule would be involved in the protonation of the enolate intermediate **3** assuming that the side chain of a conserved asparagine (Asn10/Asn12 in *Hp*-DHQ2 and *Mt*-DHQ2, respectively) would be deprotonated by WAT1.[16] However, considering the high energy required to deprotonate the side chain of an asparagine and on the basis of results from quantum mechanical (QM) calculations, this possibility was then discarded.[17] Recently, the results from computational studies of the catalytic mechanism (*Hp*-DHQ2 and *Mt*-DHQ2) in atomic detail by means of a hybrid QM/MM approach suggested that WAT1 would be mainly involved in the stabilization of the substrate and enol intermediate **3**.[17,13] Furthermore, the crystal structure of *Mt*-DHQ2 in complex with a nanomolar reversible competitive inhibitor, compound **4c**, solved at 1.5 Å shows that the oxygen atom of the methylenoxy spacer of **4c** is located 3.1 Å away from WAT1 (Figure 2).[18] The aromatic moiety of these compounds blocks the entry of the essential arginine side chain into the active site and causes a significant change in the conformation and flexibility of the loop, which is essential for the enzymatic activity. Considering that the replacement of the oxygen atom of the methylenoxy spacer of **4** by a carbon atom (ethylene spacer) leads to a decrease in the inhibition potency of up to 20-fold and that both spacers provides the necessary conformational flexibility to the aryl moiety to accommodate in the active site in an extended conformation,[19] we assume that an important contribution of the high potency of the inhibitor, which has K_i values of 42 nM[18] and 130 nM[20] against *Mt*-DHQ2 and *Hp*-DHQ2, respectively, is due to the interaction between the oxygen atom of the methylenoxy spacer with WAT1.

Structural water molecules in enzyme active sites are of interest to medicinal chemists because they can increase the binding affinity of a ligand to a protein and can provide new directions for the design of more potent inhibitors.[21] For instance, this approach has been successfully used in the development of potent HIV protease inhibitors such as a cyclic urea reported by Lam *et al.*[22] or the pyrones described by Romines *et al.*[23] or

Vara Prasad *et al*[24]. Taking into account the important stabilizing contribution that the interaction between WAT1 and either the natural substrate, the enolate intermediate **3** or enolate mimetics like compound **4c** seem to have in their binding with the DHQ2 enzyme, we decided to explore the WAT1 binding pocket in the structure-based design of inhibitors of these enzymes. The possible enhanced binding affinity of mimetics of the enolate intermediate **3** was studied by promoting interactions with WAT1 or by displacement of WAT1, causing in the latter case a direct interaction with the active site residues. To this end, we report here the synthesis of new reversible competitive inhibitors of DHQ2 from *H. pylori* and *M. tuberculosis*, namely compounds **5**–**10** (Figure 2), along with the results of inhibition studies (Figure 2). The crystal structures of DHQ2 from *M. tuberculosis* in complex with compounds **5**–**8** are also described. These structures show in detail the binding mode of these inhibitors and highlight the importance of the stereochemistry of the chiral center of the ligand side chains. Moreover, Molecular Dynamics (MD) simulation studies were carried out to study the binding mode of ligands **9**–**10** and to gain a better understanding of the binding determinants that enhance the inhibition potency.

RESULTS AND DISCUSSION

Synthesis of Compounds 5 and 6

The synthesis of the target compound **5** was performed from the previously reported allylic bromide **12**,[25] which can be prepared in five steps from commercially available (–)-quinic acid (**11**) (Scheme 2). Firstly, nucleophilic substitution of allylic bromide **12** with sodium acetate in DMF gave acetate **13**. Removal of the diacetal protecting group by treatment with aqueous trifluoroacetic acid afforded triol **10**, which was converted into the desired acid **5** by basic hydrolysis of the methyl ester **10** and subsequent protonation with Amberlite IR-120 (H^+) ion-exchange resin.

The synthesis of compound **6** was achieved by a Suzuki cross-coupling reaction between our previously reported vinyl triflate **15**[26] and vinyl boronic acid pinacol ester as the key step, followed by selective hydroboration-oxidation of the external double bond (Scheme 2). The cross-coupling reaction between vinyl

triflate **15** and vinyl boronic acid pinacol ester was performed using $Pd(PPh_3)_4$ as the catalyst in the presence of aqueous potassium carbonate, to give the cross-coupling product **16** in excellent yield. Treatment of diene **16** with borane tetrahydrofuran complex and subsequent reaction with sodium perborate gave alcohol **17**. Removal of the TBS groups with TBAF gave the triol **18**, which was converted to the desired acid **6** by basic hydrolysis and protonation with an ion-exchange resin.

Synthesis of Compounds 7–10

The synthesis of the target compounds **7–10** involved the preparation of the α,β-unsaturated ketone **19**, which was obtained by a carbonylative Suzuki cross-coupling reaction between vinyl triflate **15**[26] and commercially available B-benzyl-9-BBN using $Pd(dppf)Cl_2$ as catalyst and K_3PO_4 as base (Scheme 3). The desired hydroxyl acids **7**–**8** were obtained by 1,2-reduction of α,β-unsaturated ketones **19** or **20**, the latter being obtained by treatment of **19** with TBAF. A difference in the diastereoselectivity of the 1,2-reduction was not observed on using either TBS-protected α,β-unsaturated ketone **19** or the corresponding deprotected ketone **20**. Reduction of the two α,β-unsaturated ketones **19** and **20** gave a chromatographically separable mixture of alcohols in which the *R*-isomer was the major diastereoisomer in both cases. The stereochemistry of the reduction was confirmed by NOE experiments. Finally, the resulting lactones **23** and **24** were converted to the desired acids **7** and **8**, respectively, in the same way as compound **6** from hydroxyl lactone **18**.

The desired chloro derivatives **9** and **10** were prepared from the corresponding *R*-hydroxyl and *S*-hydroxyl derivatives **22** and **21**, respectively (Scheme 3). Treatment of alcohol **22** with triphenylphosphine and *N*-chlorosuccinimide afforded chloride **27**, which was converted to the desired acid **9** by deprotection of the TBS groups with TBAF followed by basic hydrolysis of the corresponding lactone **28** and protonation with an ion-exchange resin. Finally, compound **21** was converted to the desired acid **10** in the same way as acid **9** from hydroxyl lactone **22**.

Inhibition Assay Results

The inhibitory properties of compounds **5**–**10** against *Mt*-DHQ2 and *Hp*-DHQ2 were tested. These compounds proved to be reversible competitive inhibitors of both enzymes. The inhibition data (K_i), which were obtained from Dixon plots (1/v *vs* [I]), are summarized in Table 1.

In general, with the exception of chloride **10** (Table 1, entry 6), all of the compounds proved to be modest competitive inhibitors of both enzymes with K_i values in the micromolar range. Compounds **5** and **6** showed K_i values against *Mt*-DHQ2 and *Hp*-DHQ2 in the range 11−15 μM and 188−282 μM, respectively. The increased length of the C3 hydroxyl chain in the latter inhibitors has a more pronounced effect on the inhibitory potency against the *Hp*-DHQ2 enzyme, while only slight differences were observed for the *Mt*-DHQ2 enzyme (Table 1, entries 1 and 2). The two hydroxyl derivatives **7** and **8** showed similar K_i values in the range 27−37 μM against both enzymes (Table 1, entries 3 and 4). Compound **8**, which has an *R* configuration in the C3 side chain, proved to be slightly more potent than its epimer. The most pronounced differences were found with the chlorides **9** and **10**, which showed K_i values against *Mt*-DHQ2 and *Hp*-DHQ2 in the range 14.5−0.48 μM and 40.5−10.5 μM, respectively (Table 1, entries 5 and 6). The results show that the replacement of the hydroxyl group in compound **8** by a chloride increases the inhibitory potency against *Mt*-DHQ2 and *Hp*-DHQ2 by more than 50- and 3-fold, respectively. Chloride **10**, which has an *R* configuration on the C3 side chain, proved to be the most potent inhibitor of the series, with K_i values of 0.48 μM and 10.5 μM against *Mt*-DHQ2 and *Hp*-DHQ2, respectively. It is worth highlighting that a recent Comparative Binding Energy (COMBINE) analysis carried out with a series of competitive reversible inhibitors of *Hp*-DHQ2 and Mt-DHQ2 enzymes allowed us to quantify the interactions that contribute most significantly to explaining the key differences between the two enzymes and to quantify the importance of ligand interactions at the interface pocket between chains, which is close to the active site.[27] The latter pocket is involved in ligand efficiency and reveals significant differences between both enzymes (see Figures S7 and S8 of the Supporting Information). We believe that the significant differences in the inhibitory potency against both enzymes showed by the most potent inhibitor here reported, chloride **10**, are due to the differences in the binding interactions with the residues involved in this pocket for both enzymes.

In an effort to gain a further insight into the binding mode of these inhibitors and to identify the key binding interactions responsible for the experimentally obtained inhibition data, the crystal structures of *Mt*-DHQ2 in complex with compounds **5**–**8** were solved. The binding modes of compounds **9**–**10** with *Mt*-DHQ2 and the dynamic behavior of the key interactions identified in the binary complexes reported here were studied by MD simulation studies, the results of which are discussed below.

Structural Studies

The crystal structures of *Mt*-DHQ2 with the inhibitors **5–8** were obtained by soaking apo-*Mt*-DHQ2 crystals that were determined at 2.9, 2.2, 2.9 and 2.1 Å, respectively. All structures were determined by molecular replacement, using the previously described structure of *Mt*-DHQ2 bound to 3-hydroxyiminoquinic acid (PDB entry 1H0S)[28] as a search model and the structures were refined (Table 2). All binary complexes *Mt*-DHQ2/**5–8** contain a single *Mt*-DHQ2 molecule in the crystallographic asymmetric unit (Figure 3). The structures were refined with good geometric parameters and clear electron density is visible for all amino acids with the exception of certain residues of the flexible substrate-covering loop, a situation that is not surprising given that this flexibility is essential for the function of the enzyme (Figure S1 of the Supporting Information).

Mt-DHQ2/***5*** *Binary Complex* **–** The most remarkable features of this crystal structure are the interactions of the guanidinium group of the essential Arg19 with the C1 carboxylate group of **5** (electrostatic) and with the C3 side chain hydroxyl group of **5** (hydrogen bonding) (Figure 3A).[29] This arrangement of the side chain of Arg19 near the carboxylate group of a ligand has not been seen before in any of the available DHQ2 crystal structures and it supports the recently suggested additional role of the essential arginine as the residue that triggers the release of the product from the active site. Thus, MD simulation studies carried out in our group on the binary complex *Mt*-DHQ2/**2** indicated that the electrostatic interaction of the guanidinium group of Arg19 pulling on the carboxylate group in **2** is responsible for breaking the favorable interactions of the reaction product with the active site residues, specifically with Asn75, Ile102 and Ser103 residues.[13] As a consequence, the product is expelled from the active site after a large conformational change involving residues 101−112, which contain the conserved Arg108, Glu109 and Arg112 and 126−130. As a result of the favorable electrostatic interaction between the Arg19 side chain and the carboxylate group of **5**, the usual strong hydrogen bonding interactions

involving the side chain NH_2 group of Asn75 and the main chain NH group of Ser103 is lost as a consequence of the carboxylate rotation of ~51º (Figure 3A). This crystal structure also highlights the unusual position of WAT1 (WAT2001), which is displaced by ~1.3 Å relative to its corresponding position in the binary complex *Mt*-DHQ2/**6** (see below) towards the side chain of Asp88* of a symmetry-related neighboring enzyme subunit (Figure 3E). As a result of this displacement, the usual hydrogen bonding interaction with the carbonyl group of Pro11 residue is lost.

Mt-DHQ2/***6*** *Binary Complex* **–** In this crystal structure, Arg19 is pointing towards the active site and its guanidinium group interacts with the phenolic group of Tyr24 and the C3 side chain hydroxyl group of ligand **6** through two bridging water molecules (WAT2010 and WAT2081) (Figure 3B). Three water molecules join together the side chains of Arg19, Tyr24 and Asp88* residues. All of these attractive interactions facilitate the stabilization of the loop in the closed configuration and allow its description. In one of the possible arrangements of Asp88*, the side chain forms the usual salt bridge with the side chain of the conserved Arg112 and in the other this salt bridge is partially broken because the carboxylate group is located close to WAT1 (WAT2004). In this arrangement, WAT2004 is engaged in four hydrogen bonds, namely with the side chains of Asp88* and Asn10, the main chain amide of Gly78 and the carbonyl group of Pro11.

Mt-DHQ2/***7*** *Binary Complex* – The benzyl group of inhibitor **7** seems to block the approach of the catalytic tyrosine to Arg108, thus preventing the formation of the hydrogen-bonding interaction required to close the active site upon substrate binding (Figure 3C). The position of this group seems to be controlled by a cation-π interaction between the phenyl moiety and the guanidinium group of Arg18, which is located in the loop. Furthermore, the hydroxyl group of the inhibitor side chain establishes a good hydrogen bond with the carboxylate group of Asp88* of the neighboring subunit (2.7 Å). Notably, and in contrast to the other crystal structures reported here, electron density was not observed for the structural water molecule. This finding is not surprising considering that a water molecule in the same position would sterically clash with the C3 side chain hydroxyl group of the ligand. As discussed below, the results of MD simulation studies also suggest that the structural water molecule is not compatible with the presence of the ligand.

Mt-DHQ2/***8*** *Binary Complex* – Although the electron density is not conclusive, we modeled the side chain of Tyr24 to point inwards with the phenol group interacting with Arg108 through hydrogen-bonding with a bridging water molecule (WAT2010) (Figure 3D). As found in several binary complexes containing ligands with a C3 flexible chain substituted with an aromatic moiety, the side chain of Arg19 is probably displaced outside of the active site by the benzyl group of **8**. In contrast to its epimer, compound **7** (see above), high electron density for WAT1 (WAT2004) is observed. Moreover, a comparison of this crystal structure with that of the *Mt*-DHQ2/**4c** binary complex (PDB entry 2Y71[18]) indicates that both structures are virtually identical, with rms differences of 0.155 Å after superposition of 124 C^{α}-atom pairs (Figure 3F). In particular, the relative positions of their aromatic moieties and the oxygen atom of their C3 side chains with respect to WAT1 are very similar. Despite the structural similarities between these two binary complexes, compound **8** proved to be much less potent than compound **4c**. However, we must take into account the important differences in the aromatic moieties of the two inhibitors (phenyl *vs* 5-methylbenzo[*b*]thiophenyl) and, therefore, their different interactions with the interface pocket close to the active site. Indeed, the results of our recent QSAR studies suggest that the inhibitory potency of the ligands against the *Mt*-DHQ2 enzyme can be enhanced by establishing favorable van der Waals interactions with Glu92* of the neighboring subunit.[27] The larger size of the benzo[*b*]thiophenyl ring compared with the phenyl one favors these types of interactions (see Figure S2 of the Supporting Information). Finally, the *R*-configuration of the hydroxyl group in the C3 side chain of **8** allows it not only to establish a strong hydrogen-bonding interaction with WAT1 but also enables the appropriate positioning of the phenyl ring for a π-stacking interaction with the phenolic ring of the essential Tyr24 and an extended conformation of the flexible side chain is displayed.

Molecular Dynamics Simulation Studies

In order to analyze the relevance of the electrostatic interaction between the guanidinium group of Arg19 and the C1 carboxylate group in **5** and the hydrogen-bonding interactions with WAT1 in the reported complexes, the four binary complexes described here were subjected to 10 ns of dynamic simulation. Moreover, in order to gain further information concerning the inhibition results obtained on replacing the hydroxyl group in the C3

side chains in **7** and **8** by a chloride, the binding mode of compounds **9** and **10** in the active site of the *M. tuberculosis* enzyme was also studied by MD simulation studies. These simulations were carried out on a catalytically active trimer[30] in aqueous solution using the molecular mechanics force field AMBER.[31] Unsolved residues were modeled using the web-based ModLoop server.[32] For *Mt*-DHQ2/**5** and *Mt*-DHQ2/**7**–**8** binary complexes, the calculated loops locate the side chain of Tyr24 and Arg19 in a disposition in which they point outside of the active site in both cases. Simulations with *Mt*-DHQ2/**9**–**10** binary complexes were carried out using the enzyme coordinates found in the crystal structures of *Mt*-DHQ2 in complex with their corresponding hydroxyl derivatives **7** and **8**, with manual replacement of ligands **7**–**8** by **9**–**10**, respectively.

The MD simulation studies performed with the *Mt*-DHQ2/**5** binary complex showed that the relative position of ligand **5** and Arg19 in the active site does not change significantly during the whole simulation (10 ns) (Figure S3 of the Supporting Information). The guanidinium group of Arg19 and the C1 carboxylate group of **5** interact directly during most of the simulation and, when they do not, the two residues are linked by a bridging water molecule. These results highlight that the interactions of the guanidinium group of Arg19 with the C1 carboxylate group (electrostatic) and the primary hydroxyl group of **5** (hydrogen bonding) are very strong. More importantly, these results provide new evidence of the high mobility of the Arg19 side chain and thus the flexible loop in which it is located. This mobility enables not only control of the appropriate orientation of the essential tyrosine side chain by a cation-π interaction for the enolate generation, but also enables it to interact with the carboxylate group of the ligand. The latter interaction supports the hypothesis that the essential Arg19 is also involved in the release of the reaction product from the active site.[13] On the other hand, significant changes were not observed for the *Mt*-DHQ/**6** binary complex during the whole simulation (Figure S3 of the Supporting Information).

The computational studies carried out with *Mt*-DHQ2/**7**–**8** binary complexes revealed the importance of the stereochemistry of the chiral center of the C3 side chain in **7**–**8** for their interaction with the WAT1 binding pocket (Figure 4). Thus, for the *Mt*-DHQ2/**7** binary complex after 10 ns of simulation, WAT1 is displaced by ~1.5 Å relative to its usual position by the hydroxyl group of the C3 side chain in **7** (Figure 4A). In fact, when

the simulation studies were performed after manual removal of WAT1, the binding interactions of ligand **7** in the *Mt*-DHQ2/**7** binary complex proved to be much more stable (Figure 4B). These findings are more clearly shown in the MD simulation studies conducted with ligand **9**, in which the hydroxyl group has been replaced by a chloride. This simulation will be discussed below. In contrast, significant changes were not observed in the WAT1 binding pocket during the simulation on the *Mt*-DHQ2/**8** binary complex, which shows once again the relevance of the hydrogen-bonding interaction of the ligand with WAT1 in the binding mode of ligand **8** (Figure 4e).

The binding modes of chlorides **9** and **10** were studied using the enzyme geometries found in the crystal structures of *Mt*-DHQ2 in complex with compounds **7** and **8**. For the *Mt*-DHQ2/**9** binary complex, similar behavior was observed to that in the simulation studies conducted with the hydroxyl derivative **7** (see above), although for ligand **9** the observed displacement of WAT1 from the WAT1 binding pocket by the chloride is clearly more pronounced. The MD simulation studies conducted with *Mt*-DHQ2/**9** containing WAT1 showed that WAT1 is rapidly expelled from its usual position to be occupied by the chloride atom of ligand **9** (Figure 4C). Large movements in the bottom of the interface pocket close to the active site were observed and this is mainly because WAT1 controls the correct positioning of the Asn12 side chain, which is also establishing a strong hydrogen bond with the side chain of His63* from the neighboring enzyme subunit. These results highlight the critical structural role of WAT1 in stabilizing the region of the active site between helix 3_{10} H1 and α3´, which contain residues 10–12 and 77–79, respectively. In fact, MD simulations conducted with the apo-form of the *Mt*-DHQ2 enzyme, i.e. in the absence of ligand, showed that WAT1 is not exchanged with the bulk solvent and does not undergo significant changes during the whole simulation (Figure S4 of the Supporting Information). Moreover, when the simulations of the *Mt*-DHQ2/**9** binary complex were performed in the absence of WAT1, the binding interactions of the ligand proved to be very stable and the position of the chloride is anchored by two hydrogen-bonding interactions, one with the main chain amide of Gly78 and the other with the side chain of the conserved Asn12, and a halogen bond interaction with the carbonyl oxygen of Pro11 (Figure 4D).[33] These results suggest that when the ligand occupies the position of WAT1, part of this

stabilization is lost because the positions of residues Asn12, Pro11 and Gly78 do not seem to be as efficiently 'frozen' as they are when a water molecule is involved.

In the case of the *Mt*-DHQ2/**8** binary complex, the binding mode of inhibitor **10** in the active site of *Mt*-DHQ2 obtained by MD simulation studies showed that the substituent of the C3 side chain (chloride) in **10** interacts with WAT1 by hydrogen-bonding (Figure 4F). However, unlike ligand **8**, the chloride in **10** establishes two extra contacts, namely a halogen bond with the carbonyl oxygen of Pro11 and a CH…Cl interaction with the conserved Leu13. All of these interactions remained very stable during the whole simulation, which suggests that these interactions all contribute greatly to its binding with the enzyme and might explain the more than 50-fold higher inhibitory potency of **10** in comparison to **8**. The calculated binding free energies for both ligands also support these differences. The calculated binding free energies of compounds **9** and **10** in the active site of *Mt*-DHQ2 for the MD simulation studies conducted, using the Molecular Mechanics Poisson–Boltzmann Surface Area (MM/PBSA)[34] approach in explicit water (GB) as implemented in Amber, also support the higher affinity of chloride **10** *vs* **9** as found experimentally (Table S1 of the Supporting Information). In addition, to examine temporal changes in the enzyme structure during the 10 ns of MD simulation, the root-mean-square deviation (rmsd) with respect to the starting structure was calculated for all complexes (Figure S5 of the Supporting Information). The obtained rmsd values are between 1.3-2.7 Å and stabilize after about 0.2 ns. To determine the most deviated residues during the simulation, the rms fluctuations (rmsf) of the C^{α} atoms of the *Mt*-DHQ2 enzyme were calculated and plotted as a function of the residue number for the three chains (Figure S6 of the Supporting Information). As expected, the residues located in the substrate-covering loop, which flexibility is essential for the enzymatic activity, have the greatest rmsf values.

When considered together, the results described above suggest that the binding affinity for the DHQ2 enzyme is enhanced for those ligands that can interact with WAT1, without causing changes in the WAT1 binding pocket, and promote extra interactions with the residues located in this pocket. The replacement of the hydroxyl group in **8** by a chloride not only enhanced the hydrogen-bonding interaction with WAT1 but also favored extra

contacts with the carbonyl group of Pro11 and the side chain of Leu13, a situation that may explain its markedly higher inhibitory potency.

CONCLUSIONS AND FINAL REMARKS

Several enol mimetics, compounds **5**–**10**, of the reaction catalyzed by DHQ2, the third enzyme of the shikimic acid pathway, have been synthesized and tested as part of a structure-based design of inhibitors of DHQ2. These compounds were specifically designed to explore the WAT1 binding pocket, which has been suggested to play an important role in the stabilization of the natural substrate and the enolate intermediate **3** during the catalysis process. These compounds were synthesized by nucleophilic substitution or Suzuki cross-coupling from previously reported allylic bromide **12** or vinyl triflate **15**. The reported compounds proved to be reversible competitive inhibitors of *Mt*-DHQ2 and *Hp*-DHQ2 with K_i values in the micromolar range. Chloride **10**, which has an *R*-configuration in the C3 side chain, proved to be the most potent inhibitor of the series with a K_i value of 0.48 μM and 10.5 μM against *Mt*-DHQ2 and *Hp*-DHQ2, respectively. The results show that the replacement of the hydroxyl group (*R* configuration) of the C3 side chain in **8** by a chloride increases the inhibitory potency against *Mt*-DHQ2 and *Hp*-DHQ2 by more than 50- and 3-fold, respectively.

The crystal structures of *Mt*-DHQ2 in complex with compounds **5**–**8** were solved at 2.9, 2.2, 2.9 and 2.1 Å, respectively. The structures of these complexes show that the hydroxyl group of the C3 side chain of compounds **5**–**6** and **8** does not occupy the WAT1 binding pocket. For the *Mt*-DHQ2/**8** binary complex, this hydroxyl group interacts by hydrogen bonding with WAT1 while for the *Mt*-DHQ2/**7** binary complex, displacement of the structural water molecule and direct interaction with the enzyme was observed. Moreover, the solved crystal structure of the *Mt*-DHQ2/**5** binary complex showed an electrostatic interaction between the guanidinium group of the essential Arg19 and the carboxylate group of inhibitor **5** in the *Mt*-DHQ2/**5** binary complex. This interaction has not been seen before in any DHQ2 crystal structure. This finding supports the recently proposed additional role of Arg19 as the residue that triggers the release of the product from the active site.[13] The results of the structural and MD simulation studies reveal important differences in the binding mode interactions with WAT1 and the WAT1 binding pocket and these differences might explain the higher

inhibitory potency of the analogs with *R* configuration on the C3 side chain, i.e. compounds **8** and **10**, in comparison to their epimers, compounds **7** and **9**, which also bind to the active site with an extended conformation of this chain. This effect is particularly remarkable on replacing the OH group by a chloride. The results of MD simulation studies suggest that the OH/Cl groups of the C3 side chain in **7** and **9**, respectively, occupy the position of WAT1 in the active site. In contrast, for their epimers, compounds **8** and **10**, the OH/Cl groups interact by hydrogen bonding with WAT1 without expelling this molecule from the WAT1 binding pocket. In view of the structural and computational studies reported here, the inhibition potency against the DHQ2 enzyme would be favored by promoting interactions with WAT1, by avoiding the displacement of WAT1 and by promoting extra interactions with the residues located in the WAT1 binding pocket. In addition, those groups, which would be incorporated in the C3 side chain of the enolate mimetic with this purpose, must also allow an extended conformation of the C3 side chain in order to enable close contact of the aromatic moiety with the interface pocket between chains, which is highly involved in ligand efficiency.[27] In view of our previous results with compounds **4**,[18] the replacement of the phenyl group in **10** by a larger size ring (naphtyl or benzo[*b*]thiophenyl) would enhance binding affinity of the ligand to the enzyme. Further chemical modifications of the reported acids are required to improve internalization into *Mycobacterium tuberculosis* cell. This is currently being carried out in our laboratories through a propyl ester prodrug approach as with previously reported *O*-alkyl derivatives **4**.[18] These computational studies also highlighted the key role of WAT1 in the stabilization of the bottom of the interface pocket close to the active site and provide guidance for the future design of inhibitors against a recognized attractive target for the development of new antibacterial agents.

EXPERIMENTAL SECTION

General Procedures. All starting materials and reagents were commercially available and were used without further purification. ^{1}H NMR spectra (250, 300, 400 and 500 MHz) and ^{13}C NMR spectra (63, 75, 100 and 125 MHz) were measured in deuterated solvents. *J* values are given in Hertz. NMR assignments were carried out by a combination of 1 D, COSY, and DEPT-135 experiments. FT-IR spectra were recorded as NaCl plates or KBr discs. $[\alpha]_D^{20}$ values are given in 10^{-1} deg cm^2 g^{-1}. UV spectra and enzyme assays were performed at 25 °C using

1 cm path quartz cells in conjunction with a thermostatically controlled water bath. All procedures involving the use of ion-exchange resins were carried out at room temperature using Milli-Q deionized water. Amberlite IR-120 (H^+) (cation exchanger) was washed alternately with water, 10% NaOH, water, 10% HCl, and finally water before use.

Methyl (1*R*,3*S*,4*S*,6*R*,9*R*)-7-acetoxymethyl-3,4-dimethoxy-3,4-dimethyl-9-trimethylsilyloxy-2,5-dioxabicyclo[4.4.0]dec-7-en-9-carboxylate (13). A stirred solution of the bromide **12**[25] (300 mg, 0.64 mmol) in dry DMF (4.3 mL) was treated with sodium acetate (160 mg, 1.9 mmol). The mixture was stirred for 24 h at room temperature and diethyl ether and water were added. The organic layer was separated and the aqueous phase was extracted with diethyl ether (×2). The combined organic extracts were washed with brine. The organic extract was dried (anh. Na_2SO_4), filtered and concentrated under reduced pressure. The residue was purified by flash chromatography on silica gel, eluting with (40:60) diethyl ether/hexanes to give acetate **13** (104 mg, 36%) as a colorless oil. Starting material (164 mg, 55%) was also recovered. Corrected yield: 46%. $[\alpha]_D^{20}$= +106.8º (*c* 1.0, $CHCl_3$). ^{1}H NMR (250 MHz, $CDCl_3$) δ: 5.72 (s, 1H, H8), 4.74 (d, *J* = 13.8 Hz, 1H, C*H*HO), 4.66 (d, *J* = 13.8 Hz, 1H, CH*H*O), 4.23 (br d, *J* = 10.4 Hz, 1H, H6), 4.09–3.99 (m, 1H, H1), 3.74 (s, 3H, OCH_3), 3.27 (s, 3H, OCH_3), 3.26 (s, 3H, OCH_3), 2.21–2.09 (m, 2H, CH_2-10), 2.06 (s, 3H, CH_3), 1.31 (s, 3H, CH_3), 1.30 (s, 3H, CH_3) and 0.12 (s, 9H, $Si(CH_3)_3$) ppm. ^{13}C NMR (63 MHz, $CDCl_3$) δ: 173.8 (C), 170.5 (C), 136.0 (C), 126.0 (CH), 100.5 (C), 100.0 (C), 75.8 (C), 69.4 (CH), 65.6 (CH), 62.6 (CH_2), 52.7 (OCH_3), 48.1 (OCH_3), 48.0 (OCH_3), 37.7 (CH_2), 21.0 (CH_3), 18.0 (CH_3), 17.9 (CH_3) and 2.0 (3×CH_3) ppm. IR (film) υ: 1744 (CO) cm^{-1}. MS (ESI) *m/z* = 469 (MNa^+). HRMS calcd for $C_{20}H_{34}O_9SiNa$ (MNa^+): 469.1864; found, 469.1870.

Methyl (1*R*,4*S*,5*R*)-3-acetoxymethyl-1,4,5-trihydroxycyclohex-2-en-1-carboxylate (14). A solution of the acetal **13** (74 mg, 0.16 mmol) in a 20:1 (v/v) mixture of TFA/H_2O (0.3 mL) was stirred at 0 ºC for 15 min. Solvents were removed under reduced pressure and the crude residue was purified by flash chromatography on silica gel, eluting with (40:60) ethyl acetate/hexanes to give triol **14** (28 mg, 68%) as a colorless oil. $[\alpha]_D^{20}$= +49.3º (*c* 1.9, CH_3OH). ^{1}H NMR (250 MHz, CD_3OD) δ: 5.73 (br s, 1H, H2), 4.78 (d, *J* = 13.7 Hz, 1H, C*H*HO),

4.61 (d, *J* = 13.7 Hz, 1H, CH*H*O), 4.00–3.85 (m, 2H, H4+H5), 3.74 (s, 3H, OCH_3), 2.08 (s, 3H, CH_3) and 2.02 (m, 2H, CH_2-6) ppm. ^{13}C NMR (63 MHz, CD_3OD) δ: 176.1 (C), 172.4 (C), 140.5 (C), 126.1 (CH), 74.0 (C), 73.9 (CH), 70.6 (CH), 64.9 (OCH_2), 53.1 (OCH_3), 40.5 (CH_2) and 20.8 (CH_3) ppm. IR (film) υ: 3419 (OH) and 1732 (CO) cm^{-1}. MS (ESI) *m/z* = 283 (MNa^+). HRMS calcd for $C_{11}H_{16}O_7Na$ (MNa^+): 283.0788; found, 283.0789.

(1*R*,4*R*,5*R*)-1,4,5-Trihydroxy-3-hydroxymethylcyclohex-2-en-1-carboxylic acid (5). A solution of the ester **14** (19 mg, 0.07 mmol) in THF (0.6 mL) was treated at room temperature with an aqueous solution of LiOH (0.07 mL, 0.17 mmol, 2.5M). The mixture was stirred for 1 h, the THF was removed under reduced pressure and water was added. The aqueous layer was washed with ethyl acetate (×3) and then treated with Amberlite IR-120 (H^+) until pH 6. The resin was filtered and washed with Milli-Q water. The filtrate and the washings were lyophilized to give acid **5** (16 mg, 99%) as a yellow oil. $[\alpha]_D^{20}$ = –80.7º (*c* 1.2, CH_3OH). ^{1}H NMR (250 MHz, CD_3OD) δ: 5.68 (s, 1H, H2), 4.18 (s, 2H, OCH_2), 3.99 (d, *J* = 6.9 Hz, 1H, H4), 3.89 (m, 1H, H5) and 2.07 (m, 2H, CH_2-6) ppm. ^{13}C NMR (63 MHz, CD_3OD) δ: 179.3 (C), 143.7 (C), 125.2 (CH), 74.1 (C), 73.3 (CH), 71.1 (CH), 63.3 (OCH_2) and 39.8 (CH_2) ppm. IR (film) υ: 3434 (OH) and 1730 (CO) cm^{-1}. MS (ESI) *m/z* = 203 (M–H). HRMS calcd for $C_8H_{11}O_6$ (M–H): 203.0561; found, 203.0568.

(1*R*,4*S*,5*R*)-1,4-Di(*tert*-butyldimethylsilyloxy)-3-vinylcyclohex-2-en-1,5-carbolactone (16). A Schlenk tube was charged with triflate **15**[26] (500 mg, 0.94 mmol), $Pd(PPh_3)_4$ (115 mg, 0.1 mmol), K_2CO_3 (2.54 mL, 2.79 mmol, 1.1 M) and vinylboronic acid pinacol ester (24 µL, 1.4 mmol) in dry dioxane (11.6 mL). The resultant suspension was deoxygenated and heated at 100 ºC for 2 h under argon. The mixture was allowed to cool to room temperature. The suspension was filtered over Celite and the residue was washed with diethyl ether. The filtrate and washings were concentrated under reduced pressure to yield an oil, which was purified by flash chromatography on silica gel, eluting with (25:75) dichloromethane/hexanes, to give diene **16** (318 mg, 82%) as a colorless oil. $[\alpha]_D^{20}$ = –193.7º (*c* 1.6, $CHCl_3$). ^{1}H NMR (300 MHz, $CDCl_3$) δ: 6.14 (dd, *J* = 17.6 and 11.0 Hz, 1H, C*H*=CH_2), 5.98 (d, *J* = 1.4 Hz, 1H, H2), 5.37 (dd, *J* = 17.6 and 0.9 Hz, 1H, CH=C*H*H), 5.17 (dd, *J* = 11.0

and 0.9 Hz, 1H, CH=CH*H*), 4.56 (dd, *J* = 5.8 and 3.4 Hz, 1H, H5), 4.37 (d, *J* = 3.4 Hz, 1H, H4), 2.44 (d, *J* = 10.6 Hz, 1H, $H6_{ax}$), 2.35 (ddd, *J* = 10.6, 5.8 and 1.9 Hz, 1H, $H6_{eq}$), 0.93 (s, 9H, $C(CH_3)_3$), 0.89 (s, 9H, $C(CH_3)_3$), 0.19 (s, 3H, CH_3), 0.16 (s, 6H, 2×CH_3) and 0.15 (s, 3H, CH_3) ppm. ^{13}C NMR (75 MHz, $CDCl_3$) δ: 175.6 (C), 136.8 (C), 134.7 (CH), 133.8 (CH), 116.3 (CH_2), 75.9 (CH), 75.1 (C), 66.0 (CH), 37.1 (CH_2), 25.8 ($C(CH_3)_3$), 25.8 ($C(CH_3)_3$), 18.2 (2×$C(CH_3)_3$), –2.9 (2×CH_3), –3.9 (CH_3) and –4.4 (CH_3) ppm. IR (film) υ: 1801 (CO) cm^{-1}. MS (ESI) *m/z* = 433 (MNa^+). HRMS calcd for $C_{21}H_{38}O_4Si_2Na$ (MNa^+): 433.2201; found, 433.2178.

(1*R*,4*S*,5*R*)-1,4-Di(*tert*-butyldimethylsilyloxy)-3-(2-hydroxy)ethylcyclohex-2-en-1,5-carbolactone (17). A stirred solution of diene **16** (50 mg, 0.12 mmol) in dry THF (3 mL), under argon at 0 ºC, was treated with a BH_3-THF solution (1.22 mL, 1.22 mmol). The mixture was stirred for 1 h. An aqueous solution of $NaBO_3$ (3 mL, 1.22 mmol, 0.4 M) was added and the resulting solution was stirred for 2 h at this temperature. The mixture was warmed up to room temperature and ethyl acetate and water were added. The organic layer was separated and the aqueous layer was extracted with ethyl acetate (×2). The combined organic extracts were dried (anh. Na_2SO_4), filtered and concentrated under reduced pressure. The residue was purified by flash chromatography on silica gel, eluting with (50:50) diethyl ether/hexanes, to give alcohol **17** (18 mg, 35%) as a colorless oil. $[\alpha]_D^{20}$ = +132.8º (*c* 1.8, $CHCl_3$). ^1H NMR (300 MHz, $CDCl_3$) δ: 5.84 (br d, *J* = 1.1 Hz, 1H, H2), 4.48 (m, 1H, H5), 4.06 (d, *J* = 3.1 Hz, 1H, H4), 3.72 (td, *J* = 6.5 and 1.7 Hz, 2H, CH_2O), 2.33–2.31 (m, 4H, 2×CH_2), 1.57 (s, 1H, OH), 0.92 (s, 9H, $C(CH_3)_3$), 0.91 (s, 9H, $C(CH_3)_3$), 0.18 (s, 3H, CH_3), 0.16 (s, 3H, CH_3), 0.15 (s, 3H, CH_3) and 0.14 (s, 3H, CH_3) ppm. ^{13}C NMR (75 MHz, $CDCl_3$) δ: 176.1 (C), 136.1 (C), 133.1 (CH), 76.0 (CH), 74.8 (C), 68.2 (CH), 61.0 (CH_2), 37.2 (CH_2), 35.2 (CH_2), 25.8 ($C(CH_3)_3$), 25.7 ($C(CH_3)_3$), 18.1 ($C(CH_3)_3$), 18.0 ($C(CH_3)_3$), –2.9 (CH_3), –2.9 (CH_3), –4.5 (CH_3) and –4.5 (CH_3) ppm. IR (film) υ: 3421 (OH) and 1794 (CO) cm^{-1}. MS (ESI) *m/z* = 451 (MNa^+). HRMS calcd for $C_{21}H_{40}O_5Si_2Na$ (MNa^+): 451.2306; found, 451.2305.

(1*R*,4*S*,5*R*)-1,4-Dihydroxy-3-(2-hydroxy)ethylcyclohex-2-en-1,5-carbolactone (18). Tetrabutylammonium fluoride (0.5 mL, 0.47 mmol, *ca* 1.0 M in THF) was added to a stirred solution of the silyl ether **17** (82 mg, 0.19 mmol) in dry THF (2.7 mL) under argon at 0 ºC. The mixture was stirred for 2 h and water and ethyl acetate

were added. The aqueous layer was acidified with dilute HCl (10%) and the organic layer was separated. The aqueous phase was extracted with ethyl acetate (x2). The combined organic extracts were dried (anh. Na_2SO_4), filtered and concentrated under reduced pressure. The residue was purified by flash chromatography on silica gel, eluting with (80:20) ethyl acetate-hexanes to yield triol **18** (24 mg, 63%) as a colorless oil. $[\alpha]_D^{20} = -232^o$ (*c* 1.5, MeOH). ^{1}H NMR (300 MHz, CD_3OD) δ: 5.83 (br s, 1H, H2), 4.59 (ddd, *J* = 5.2, 3.2 and 0.8 Hz, 1H, H5), 4.03 (d, *J* = 3.2 Hz, 1H, H4), 3.68 (dd, *J* = 7.0 and 2.2 Hz, 1H, OC*H*H), 3.66 (dd, *J* = 7.0 and 2.8 Hz, 1H, OCH*H*) and 2.44–2.23 (m, 4H, 2×CH_2) ppm. ^{13}C NMR (63 MHz, CD_3OD) δ: 179.1 (C), 138.7 (C), 132.3 (CH), 77.9 (CH), 74.0 (C), 68.0 (CH), 61.3 (CH_2), 37.4 (CH_2) and 36.4 (CH_2) ppm. IR (film) υ: 3366 (OH) and 1778 (CO) cm^{-1}. MS (ESI) *m/z* = 223 (MNa^+). HRMS calcd for $C_9H_{12}O_5Na$ (MNa^+): 223.0577; found, 223.0571.

(1*R*,4*R*,5*R*)-1,4,5-Trihydroxy-3-(2-hydroxy)ethylcyclohex-2-ene-1-carboxylic acid (6). A solution of the lactone **18** (15 mg, 0.08 mmol) in THF (0.8 mL) and aqueous lithium hydroxide (0.4 mL, 0.2 mmol, 0.5 M) was stirred at room temperature for 1 h. Water was added and the THF was removed under reduced pressure. The resulting aqueous solution was washed with ethyl acetate (×2) and the aqueous extract was treated with Amberlite IR-120 (H^+) until pH 6. The resin was filtered off and washed with Milli-Q water. The filtrate and the washings were lyophilized to give acid **6** (12 mg, 75%) as a colorless oil. $[\alpha]_D^{20} = -63^o$ (*c* 1.2, H_2O). ^{1}H NMR (300 MHz, D_2O) δ: 5.60 (br s, 1H, H2), 4.05 (d, *J* = 8.0 Hz, 1H, H4), 3.92 (m, 1H, H5), 3.75 (t, *J* = 6.5 Hz, 2H, OCH_2), 2.55 (m, 1H, C*H*H), 2.34 (m, 1H, CH*H*) and 2.18–2.07 (m, 2H, CH_2) ppm. ^{13}C NMR (63 MHz, D_2O) δ: 178.8 (C), 142.2 (C), 124.9 (CH), 73.9 (C), 73.6 (CH), 69.9 (CH), 60.2 (CH_2), 39.4 (CH_2) and 35.1 (CH_2) ppm. IR (film) υ: 3339 (OH) and 1708 (CO) cm^{-1}. MS (ESI) *m/z* = 217 (M–H). HRMS calcd for $C_9H_{13}O_6$ (M–H): 217.0708; found, 217.0714.

Carbonylation of triflate 15. A stirred solution of triflate **15**[22] (813 mg, 1.52 mmol), Pd(dppf)Cl_2 (86 mg, 0.11 mmol) in dry THF (150 mL) saturated with a continuous flow of carbon monoxide was treated with B-benzyl-9-BBN (8.25 mL, 4.13 mmol, *ca.* 0.5M in THF) and an aqueous solution of K_3PO_4 (4 mL, 4 mmol, 1M). The resulting mixture was heated at 55 ºC for 4 h. The mixture was allowed to cool to room temperature, the organic

solvent was removed under reduced pressure and the mixture was diluted with diethyl ether and water. The organic layer was separated and the organic phase was extracted with diethyl ether (×2). The combined organic extracts were dried (anh. Na_2SO_4), filtered and concentrated under reduced pressure. The residue was purified by flash chromatography, eluting with (5:95) diethyl ether/hexanes to give ketone **19** (385 mg, 51%) as a white solid. The corresponding cross-coupling product was also obtained in 13% yield (93 mg). Data for **19**: White solid. Mp: 80–81 ºC. $[\alpha]_D^{20}$= –15.8º (*c*1.0, $CHCl_3$). ^{1}H NMR (400 MHz, $CDCl_3$) δ: 7.30 (m, 2H, 2×ArH), 7.24 (m, 1H, ArH), 7.17 (d, *J* = 7.3 Hz, 2H, 2×ArH), 6.88 (d, *J* = 0.9 Hz, 1H, H2), 4.68 (d, *J* = 3.4 Hz, 1H, H4), 4.55 (dd, *J* = 5.7 and 3.5 Hz, 1H, H5), 3.92 (br d, *J* = 15.7 Hz, 1H, C*H*HPh), 3.89 (br d, *J* = 15.7 Hz, 1H, CH*H*Ph), 2.48 (d, *J* = 10.9 Hz, 1H, $H6_{ax}$), 2.38 (m, 1H, $H6_{eq}$), 0.94 (s, 9H, $C(CH_3)_3$), 0.83 (s, 9H, $C(CH_3)_3$), 0.17 (s, 3H, CH_3), 0.17 (s, 3H, CH_3), 0.12 (s, 3H, CH_3) and 0.06 (s, 3H, CH_3) ppm. ^{13}C NMR (75 MHz, $CDCl_3$) δ: 196.2 (C), 174.4 (C), 144.9 (CH), 138.5 (C), 134.0 (C), 129.4 (2×CH), 128.9 (2×CH), 127.1 (CH), 75.7 (CH), 75.2 (C), 63.5 (CH), 45.0 (CH_2), 36.4 (CH_2), 25.8 ($C(CH_3)_3$), 25.7 ($C(CH_3)_3$), 18.1 ($C(CH_3)_3$), 18.1 ($C(CH_3)_3$), –3.0 (2×CH_3), –4.8 (CH_3) and –5.1 (CH_3) ppm. IR (KBr) υ: 1801 (CO) and 1684 (CO) cm^{-1}. MS (ESI) *m/z* = 525 (MNa^+). HRMS calcd for $C_{27}H_{42}O_5Si_2Na$ (MNa^+): 525.2463; found, 525.2449. Data for cross-coupling product [(1*R*,4*R*,5*R*)-1,4-di(*tert*-butyldimethylsilyloxy)-3-benzylcyclohex-2-en-1,5-carbolactone]: Colorless oil. $[\alpha]_D^{20}$= –16.2º (*c*1.0, $CHCl_3$). ^{1}H NMR (300 MHz, $CDCl_3$) δ: 7.29 (m, 2H, 2×ArH), 7.21 (m, 1H, ArH), 7.09 (d, *J* = 7.1 Hz, 2H, 2×ArH), 5.54 (s, 1H, H2), 4.48 (m, 1H, H5), 4.02 (d, *J* = 3.0 Hz, 1H, H4), 3.46 (d, *J* = 16.1 Hz, 1H, C*H*HPh), 3.28 (d, *J* = 16.1 Hz, 1H, CH*H*Ph), 2.34 (m, 2H, CH_2-6), 0.93 (s, 9H, $C(CH_3)_3$), 0.87 (s, 9H, $C(CH_3)_3$), 0.10 (s, 6H, 2×CH_3), 0.09 (s, 3H, CH_3) and 0.06 (s, 3H, CH_3) ppm. ^{13}C NMR (100 MHz, $CDCl_3$) δ: 176.0 (C), 138.8 (C), 137.3 (C), 132.7 (CH), 129.2 (2×CH), 128.5 (2×CH), 126.5 (CH), 75.9 (CH), 74.8 (C), 67.5 (CH), 38.2 (CH_2), 37.4 (CH_2), 25.7 ($C(CH_3)_3$), 25.6 ($C(CH_3)_3$), 17.9 ($C(CH_3)_3$), 17.9 ($C(CH_3)_3$), –3.1 (2×CH_3), –4.5 (CH_3) and –4.7 (CH_3) ppm. IR (film) υ: 1805 (C=O) cm^{-1}. MS (ESI) *m/z* = 497 (MNa^+). HRMS calcd for $C_{26}H_{42}O_4Si_2Na$ (MNa^+): 497.2514; found, 497.2523.

(1*R*,4*R*,5*R*)-1,4-Dihydroxy-3-(2-benzylacetyl)cyclohex-2-en-1,5-carbolactone (20). A stirred solution of the silylether **19** (385 mg, 0.77 mmol) in dry THF (7.7 mL), under argon at 0 ºC, was treated with

tetrabutylammonium fluoride (1.92 mL, 1.92 mmol, *ca.* 1.0 M in THF). The mixture was stirred for 30 min, saturated NH_4Cl was added and the organic layer was extracted with diethyl ether (×3). The combined organic extracts were dried (anh. Na_2SO_4), filtered and concentrated under reduced pressure. The crude product was purified by flash chromatography on silica gel, eluting with (1:1:1) diethyl ether/acetone/hexanes to give diol **20** (60 mg, 29%) as a white solid. $[\alpha]_D^{20} = -15.0^{\circ}$ (*c*1.0, CH_3OH). Mp: 172–173 ºC. ^{1}H NMR (300 MHz, CD_3OD) δ: 7.29 (m, 2H, 2×ArH), 7.23 (m, 1H, ArH), 7.18 (m, 2H, 2×ArH), 7.13 (br s, 1H, H2), 4.69 (m, 1H, H5), 4.59 (d, *J* = 3.4 Hz, 1H, H4), 4.07 (d, *J* = 16.2 Hz, 1H, C*H*HPh), 4.00 (d, *J* = 16.2 Hz, 1H, CH*H*Ph) and 2.41 (m, 2H, CH_2-6) ppm. ^{13}C NMR (100 MHz, CH_3OD) δ: 198.9 (C), 177.1 (C), 145.5 (CH), 139.6 (C), 135.7 (C), 130.6 (2×CH), 129.5 (2×CH), 127.8 (CH), 77.4 (CH), 74.4 (C), 64.2 (CH), 45.6 (CH_2) and 36.7 (CH_2) ppm. IR (KBr) υ: 3457 (OH), 3420 (OH), 1766 (CO) and 1680 (CO) cm^{-1}. MS (ESI) *m/z*: 297 (MNa^+). HRMS calcd for $C_{15}H_{14}O_5Na$ (MNa^+): 297.0733; found, 297.0736.

Reduction of α,β-unsaturated 19. A stirred solution of the ketone **19** (100 mg, 0.20 mmol) in dry THF (2 mL), under argon at 0 ºC, was treated with cerium(III) chloride heptahydratate (127 mg, 0.60 mmol), sodium borohydride (3.2 mg, 0.08 mmol) and methanol (5 drops). The mixture was stirred for 1 h and water and diethyl ether were added. The organic layer was separated and the aqueous layer was extracted with diethyl ether (×3). The combined organic extracts were dried (anh. Na_2SO_4), filtered and concentrated under reduced pressure. The crude product was purified by flash chromatography on silica gel, eluting with (5:5:90) diethyl ether/dichloromethane/hexanes to give alcohol **21** (28 mg, 28%) and alcohol **22** (51 mg, 51%). Data for (1*R*,4*R*,5*R*)-1,4-di(*tert*-butyldimethylsilyloxy)-3-[(1*S*)-1-hydroxy-2-phenyl]ethylcyclohex-2-en-1,5-carbolactone (**21**). White solid. $[\alpha]_D^{20} = -12.3^{\circ}$ (*c*1.0, $CHCl_3$). ^{1}H NMR (300 MHz, $CDCl_3$) δ: 7.34–7.24 (m, 3H, 3×ArH), 7.14 (m, 1H, ArH), 6.03 (s, 1H, H2), 4.47 (q, *J* = 3.2 Hz, 1H, H5), 4.43 (m, 1H, C*H*OH), 4.09 (d, *J* = 3.3 Hz, 1H, H4), 2.94 (dd, *J* = 13.6 and 5.0 Hz, 1H, C*H*HPh), 2.79 (dd, *J* = 13.6 and 7.9 Hz, 1H, CH*H*Ph), 2.33 (d, *J* = 2.6 Hz, 2H, CH_2-6), 0.92 (s, 9H, $C(CH_3)_3$), 0.91 (s, 9H, $C(CH_3)_3$), 0.18 (s, 3H, CH_3), 0.16 (s, 3H, CH_3), 0.14 (s, 3H, CH_3) and 0.12 (s, 3H, CH_3) ppm. ^{13}C NMR (63 MHz, $CDCl_3$) δ: 175.7 (C), 141.0 (C), 136.9 (C), 131.6 (CH), 129.7 (2×CH), 128.8 (2×CH), 127.0 (CH), 75.9 (CH), 74.9 (C), 70.9 (CH), 66.6 (CH), 43.0 (CH_2),

37.1 (CH_2), 25.8 ($C(CH_3)_3$), 25.8 ($C(CH_3)_3$), 18.2 ($C(CH_3)_3$), 18.0 ($C(CH_3)_3$), –2.9 (2×CH_3) and –4.3 (2×CH_3) ppm. IR (KBr) υ: 3421 (OH) and 1792 (CO) cm^{-1}. MS (ESI) *m/z* = 597 (MNa^+). HRMS calcd for $C_{27}H_{44}O_5Si_2Na$ (MNa^+): 527.2619; found, 527.2624. Data for (1*R*,4*R*,5*R*)-1,4-di(*tert*-butyldimethylsilyloxy)-3-[(1*R*)-1-hydroxy-2-phenyl]ethylcyclohex-2-en-1,5-carbolactone (**22**). Colorless oil. $[\alpha]_D^{20}$= –37.2º (*c*1.0, $CHCl_3$). ^{1}H NMR (300 MHz, $CDCl_3$) δ: 7.34–7.23 (m, 3H, 3×ArH), 7.18 (m, 2H, 2×ArH), 5.95 (s, 1H, H2), 4.51 (q, *J* = 3.1 Hz, 1H, H5), 4.42 (d, *J* = 3.2 Hz, 1H, H4), 4.33 (m, 1H, C*H*OH), 3.02 (dd, *J* = 13.7 and 4.5 Hz, 1H, C*H*HPh), 2.83 (dd, *J* = 13.7 and 8.7 Hz, 1H, CH*H*Ph), 2.35 (d, *J* = 2.6 Hz, 2H, CH_2-6), 0.93 (s, 9H, $C(CH_3)_3$), 0.91 (s, 9H, $C(CH_3)_3$), 0.19 (s, 3H, CH_3), 0.18 (s, 3H, CH_3), 0.15 (s, 3H, CH_3) and 0.12 (s, 3H, CH_3) ppm. ^{13}C NMR (63 MHz, $CDCl_3$) δ: 175.5 (C), 139.5 (C), 137.7 (C), 133.2 (CH), 129.5 (2×CH), 128.8 (2×CH), 126.8 (CH), 75.9 (CH), 74.8 (C), 72.3 (CH), 66.6 (CH), 42.1 (CH_2), 37.1 (CH_2), 25.9 ($C(CH_3)_3$), 25.7 ($C(CH_3)_3$), 18.2 ($C(CH_3)_3$), 18.0 ($C(CH_3)_3$), –2.9 (2×CH_3), –4.3 (CH_3) and –4.4 (CH_3) ppm. IR (film) υ: 3417 (OH) and 1791 (CO) cm^{-1}. MS (ESI) *m/z* = 527 (MNa^+). HRMS calcd for $C_{27}H_{44}O_5Si_2Na$ (MNa^+): 527.2619; found, 527.2625.

Reduction of α,β-unsaturated ketone 20. A stirred solution of the ketone **20** (43 mg, 0.16 mmol) in dry THF (4 mL), under argon at 0 ºC, was treated with cerium(III) chloride heptahydratate (59 mg, 0.16 mmol), sodium triacetoxyborohydride (110 mg, 0.52 mmol) and methanol (5 drops). The mixture was stirred for 1 h and water and ethyl acetate were added. The organic layer was separated and the aqueous layer was extracted with ethyl acetate (×3). The combined organic extracts were dried (anh. Na_2SO_4), filtered and concentrated under reduced pressure. The crude product was purified by HPLC on a Luna phenomenex C_{18} column eluting with acetonitrile/water (48:52) at 7 mL·min^{-1} to give triols **23** (10 mg, 26%) and **24** (22 mg, 51%), both as white solids. Data for (1*R*,4*R*,5*R*)-1,4-dihydroxy-3-[(1*S*)-1-hydroxy-2-phenylacetyl]cyclohex-2-en-1,5-carbolactone (**23**). White solid. $[\alpha]_D^{20}$= –18.1º (*c*1.0, CH_3OH). Mp: 170–171 ºC. ^{1}H NMR (250 MHz, CD_3OD) δ: 7.28–7.14 (m, 5H, 5×ArH), 5.90 (s, 1H, H2), 4.61 (q, *J* = 3.2 1H, H5), 4.36 (m, 2H, H4+C*H*OH), 2.97 (dd, *J* = 13.7 and 5.2 Hz, 1H, C*H*HPh), 2.84 (d, *J* = 13.7 and 8.3 Hz, 1H, CH*H*Ph) and 2.32 (m, 2H, CH_2-6) ppm. ^{13}C NMR (63 MHz, CH_3OD) δ: 178.6 (C), 142.2 (C), 139.9 (C), 132.0 (CH), 130.5 (2×CH), 129.2 (2×CH), 127.2 (CH), 77.8

(CH), 74.0 (C), 73.9 (CH), 66.6 (CH), 43.0 (CH_2) and 37.5 (CH_2) ppm. IR (KBr) υ: 3402 (OH), 3418 (OH) and 1765 (CO) cm^{-1}. MS (ESI) *m/z* = 299 (MNa^+). HRMS calcd for $C_{15}H_{16}O_5Na$ (MNa^+): 299.0890; found, 299.0891. Data for (1*R*,4*R*,5*R*)-1,4-dihydroxy-3-[(1*R*)-1-hydroxy-2-phenylacetyl]cyclohex-2-en-1,5-carbolactone (**24**). White solid. $[\alpha]_D^{20} = -7.8^{\circ}$ (*c*1.0, CH_3OH). Mp: 138–139 ºC. ^{1}H NMR (250 MHz, CD_3OD) δ: 7.27–7.15 (m, 5H, 5×ArH), 5.96 (s, 1H, H2), 4.57 (m, 1H, H5), 4.50 (m, 1H, C*H*OH), 4.02 (d, *J* = 2.7 Hz, 1H, H4), 2.97 (dd, *J* = 13.5 and 5.2 Hz, 1H, C*H*HPh), 2.79 (dd, *J* = 13.5 and 7.3 Hz, 1H, CH*H*Ph) and 2.28 (m, 2H, CH_2-6) ppm. ^{13}C NMR (63 MHz, CH_3OD) δ: 178.8 (C), 143.7 (C), 139.4 (C), 130.9 (CH), 130.7 (2×CH), 129.2 (2×CH), 127.2 (CH), 78.0 (CH), 74.1 (C), 72.1 (CH), 66.4 (CH), 43.8 (CH_2) and 37.3 (CH_2) ppm. IR (KBr) υ: 3416 (OH) and 1781 (CO) cm^{-1}. MS (ESI) *m/z* = 299 (MNa^+). HRMS calcd for $C_{15}H_{16}O_5Na$ (MNa^+): 299.0890; found, 299.0882.

(1*R*,4*R*,5*R*)-1,4,5-Trihydroxy-3-[(1*S*)-1-hydroxy-2-phenylethyl]cyclohex-2-en-1-carboxylic acid (7). A solution of carbolactone **23** (10.5 mg, 0.04 mmol) in THF (0.4 mL) and aqueous lithium hydroxide (0.1 mL, 0.10 mmol, 1 M) was stirred at room temperature for 30 min. Water was added and the THF was removed under reduced pressure. The resulting aqueous solution was washed with diethyl ether (×3) and the aqueous extract was treated with Amberlite IR-120 (H^+) until pH 6. The resin was filtered off and washed with Milli-Q water. The filtrate and the washings were lyophilized to give acid **7** (10 mg, 90%) as a white solid. $[\alpha]_D^{20} = -6.0^{\circ}$ (*c*1.0, MeOH). Mp: 132–133 ºC. ^{1}H NMR (250 MHz, D_2O) δ: 7.43–7.29 (m, 5H, 5×ArH), 5.78 (s, 1H, H2), 4.59 (dd, *J* = 9.2 and 4.5 Hz, 1H, C*H*OH), 4.27 (d, *J* = 7.5 Hz, 1H, H4), 3.97 (q, *J* = 7.5 Hz, 1H, H5), 3.12 (dd, *J* = 13.9 and 4.5 Hz, 1H, CH*H*Ph), 2.90 (dd, *J* = 13.9 and 9.2 Hz 1H, C*H*HPh) and 2.11 (d, *J* = 7.5 Hz, 2H, CH_2-6) ppm. ^{13}C NMR (63 MHz, D_2O) δ: 179.4 (C), 144.3 (C), 139.2 (C), 129.8 (2×CH), 129.0 (2×CH), 126.9 (CH), 125.7 (CH), 73.7 (C), 72.5 (2×CH), 69.9 (CH), 41.7 (CH_2) and 38.6 (CH_2) ppm. IR (KBr) υ: 3367 (OH) and 1721 (CO) cm^{-1}. MS (ESI) *m/z* = 293 (M–H). HRMS calcd for $C_{15}H_{17}O_6$ (M–H): 293.1031; found, 293.1029.

(1*R*,4*R*,5*R*)-1,4,5-Trihydroxy-3-[(1*R*)-1-hydroxy-2-phenylethyl]cyclohex-2-en-1-carboxylic acid (8). A solution of carbolactone **24** (7 mg, 0.025 mmol) in THF (0.4 mL) and aqueous lithium hydroxide (0.09 mL,

0.09 mmol, 1 M) was stirred at room temperature for 30 min. Water was added and the THF was removed under reduced pressure. The resulting aqueous solution was washed with diethyl ether (×3) and the aqueous extract was treated with Amberlite IR-120 (H^+) until pH 6. The resin was filtered off and washed with Milli-Q water. The filtrate and the washings were lyophilized to give acid **8** (5 mg, 67%) as a white solid. $[\alpha]_D^{20} = -1.1^\circ$ (*c*1.0, MeOH). Mp: 95–96 ºC. NMR (300 MHz, D_2O) δ: 7.39 (m, 2H, 2×ArH), 7.32 (m, 23H, 3×ArH), 5.70 (s, 1H, H2), 4.08 (d, *J* = 7.8 Hz, 1H, H4), 3.95 (m, 1H, H5), 3.61 (m, 1H, C*H*OH), 3.16 (dd, *J* = 14.0 and 4.0 Hz, 1H, CH*H*Ph), 2.74 (dd, *J* = 14.0 and 8.4 Hz 1H, C*H*HPh) and 2.14 (m, 2H, CH_2-6) ppm. ^{13}C NMR (63 MHz, D_2O) δ: 178.5 (C), 146.0 (C), 138.6 (C), 130.0 (2×CH), 128.9 (2×CH), 127.0 (CH), 122.4 (CH), 73.6 (C), 72.6 (CH), 70.8 (CH), 69.9 (CH), 41.7 (CH_2) and 38.6 (CH_2) ppm. IR (KBr) υ: 3430 (OH) and 1721 (CO) cm^{-1}. MS (ESI) *m/z* = 293 (M–H). HRMS calcd for $C_{15}H_{17}O_6$ (M–H): 293.1031; found, 293.1029.

(1*R*,4*R*,5*R*)-1,4-Di(*tert*-butyldimethylsilyloxy)-3-[(1*R*)-1-chloro-2-phenyl]ethylcyclohex-2-en-1,5-carbolactone (25). A stirred solution of the alcohol **21** (112 mg, 0.22 mmol) in dry THF (10 mL), at room temperature and under argon, was treated with *N*-chlorosuccinimide (59 mg, 0.44 mmol) and triphenylphosphine (87 mg, 0.33 mmol). The reaction mixture was stirred for 1 h and the solvent was removed under reduced pressure. The crude product was purified by flash chromatography on silica gel, eluting with diethyl ether/hexanes (5:95), to give chloride **25** (48 mg, 42%) as a white foam. $[\alpha]_D^{20} = -41.7$ (*c* 1.0, $CHCl_3$). ^{1}H NMR (250 MHz, $CDCl_3$) δ: 7.35–7.18 (m, 5H, 5×ArH), 6.10 (s, 1H, H2), 4.66 (dd, *J* = 9.3 and 5.3 Hz, 1H, CHCl), 4.53 (dd, *J* = 5.6 and 3.2 Hz,1H, H5), 4.44 (d, *J* = 3.2 Hz, 1H, H4), 3.30 (dd, *J* = 14.3 and 5.3 Hz, 1H, C*H*HPh), 3.15 (dd, *J* = 14.3 and 9.3 Hz, 1H, CH*H*Ph), 2.37 (ddd, *J* = 10.6, 5.6 and 1.5 Hz, 1H, $H6_{eq}$), 2.27 (d, *J* = 10.6 Hz, 1H, $H6_{ax}$), 0.92 (s, 9H,$C(CH_3)_3$), 0.91 (s, 9H,$C(CH_3)_3$), 0.18 (s, 3H, CH_3), 0.16 (s, 6H, 2xCH_3) and 0.09 (s, 3H, CH_3) ppm. ^{13}C NMR (63 MHz, $CDCl_3$) δ: 175.1 (C), 138.5 (C), 137.6 (C), 133.4 (CH), 129.1 (2×CH), 128.6 (2×CH), 127.0 (CH), 75.7 (CH), 75.1 (C), 66.1 (CH), 57.9 (CH), 40.8 (CH_2), 37.4 (CH_2), 25.8 ($C(CH_3)_3$), 25.7 ($C(CH_3)_3$), 18.2 ($C(CH_3)_3$), 18.0 ($C(CH_3)_3$), –3.0 (2×CH_3), –4.5 (CH_3) and –4.6 (CH_3) ppm. IR (film): 1805 (CO) cm^{-1}. MS (ESI) *m/z* (%) 545 (MNa^+). HRMS calcd for $C_{27}H_{43}O_4ClNa$ (MNa^+): 545.2281; found, 545.2250.

(1*R*,4*R*,5*R*)-1,4-Dihydroxy-3-[(1*R*)-1-chloro-2-phenyl]ethylcyclohex-2-en-1,5-carbolactone (26). A stirred solution of the silylether **25** (32 mg, 0.06 mmol) in dry THF (1.0 mL), under argon at 0 ºC, was treated with tetrabutylammonium fluoride (0.15 mL, 0.05 mmol, *ca.* 1.0 M in THF). The mixture was stirred for 15 min, saturated NH_4Cl was added and the organic layer was extracted with diethyl ether (×3). The combined organic extracts were dried (anh. Na_2SO_4), filtered and concentrated under reduced pressure. The crude product was purified by flash chromatography on silica gel, eluting with (1:1:2) diethyl ether/acetone/hexanes, to give diol **26** (14 mg, 79%) as a white foam. $[\alpha]_D^{20} = -6.9$ (*c* 1.0, $CHCl_3$). ^{1}H NMR (300 MHz, $CDCl_3$) δ: 7.36–7.28 (m, 4H, 4×ArH), 7.18 (m, 1H, ArH), 6.08 (s, 1H, H2), 4.75 (m, 1H, CHCl), 4.70 (m, 1H, H5), 4.57 (d, *J* = 3.3 Hz, 1H, H4), 3.29 (dd, *J* = 14.0 and 6.4 Hz, 1H, C*H*HPh), 3.20 (dd, *J* = 14.0 and 8.3 Hz, 1H, CH*H*Ph), 2.49 (d, *J* = 11.2 Hz, 1H, $H6_{ax}$) and 2.38 (ddd, *J* = 11.2, 5.8 and 1.8 Hz, 1H, $H6_{eq}$) ppm. ^{13}C NMR (63 MHz, CD_3OD) δ: 178.1 (C), 141.0 (C), 139.2 (C), 133.4 (CH), 130.3 (2×CH), 129.4 (2×CH), 127.8 (CH), 77.7 (CH), 74.2 (C), 66.3 (CH), 60.3 (CH), 42.3 (CH_2) and 37.5 (CH_2) ppm. IR (film): 3422 (OH) and 1782 (CO) cm^{-1}. MS (ESI) *m/z* (%) 317 (MNa^+). HRMS calcd for $C_{15}H_{15}O_4ClNa$ (MNa^+): 317.0551; found, 317.0575.

(1*R*,4*R*,5*R*)-1,4,5-Trihydroxy-3-[(1*R*)-1-chloro-2-phenyl]ethylcyclohex-2-en-1-carboxylic acid (10). A solution of carbolactone **26** (14 mg, 0.05 mmol) in THF (3.0 mL) at 0 ºC was treated with aqueous lithium hydroxide (0.06 mL, 0.06 mmol, 1 M) and the mixture was stirred for 2 h. Water was added and the THF was removed under reduced pressure. The resulting aqueous solution was washed with diethyl ether (×3) and the aqueous extract was treated with Amberlite IR-120 (H^+) until pH 6. The resin was filtered off and washed with Milli-Q water. The filtrate and the washings were lyophilized to give acid **10** (2.9 mg, 23%) as a white solid. $[\alpha]_D^{20} = -1.7$ (*c* 1.0, MeOH). ^{1}H NMR (500 MHz, D_2O) δ: 7.40 (m, 2H, 2×ArH), 7.34 (m, 3H, 3×ArH), 5.79 (s, 1H, H2), 4.59 (dd, *J* = 9.1 and 4.4 Hz, 1H, CHCl), 4.27 (d, *J* = 7.4 Hz,1H, H4), 3.97 (m, 1H, H5), 3.13 (dd, *J* = 14.0 and 4.4 Hz, 1H, C*H*HPh), 2.90 (dd, *J* = 14.0 and 9.1 Hz, 1H, CH*H*Ph), and 2.11 (m, 2H, CH_2-6) ppm. ^{13}C NMR (63 MHz, D_2O) δ: 162.0 (C), 145.1 (C), 139.3 (C), 130.0 (2×CH), 129.2 (2×CH), 127.2 (CH), 125.1 (CH), 73.6 (C), 72.9 (CH), 72.8 (CH), 69.9 (CH), 41.9 (CH_2) and 38.8 (CH_2) ppm. IR (film): 3399 (OH) and

1685 (CO) cm^{-1}. MS (ESI) *m/z* (%) 311 (M–H). HRMS calcd for $C_{15}H_{17}O_5Cl$ (M–H): 311.1085; found, 311.1087.

(1*R*,4*R*,5*R*)-1,4-Di(*tert*-butyldimethylsilyloxy)-3-[(1*S*)-1-chloro-2-phenyl]ethylcyclohex-2-en-1,5-carbolactone (27). A stirred solution of the alcohol **22** (143 mg, 0.29 mmol) in dry THF (10 mL), at room temperature and under argon, was treated with *N*-chlorosuccinimide (77 mg, 0.58 mmol) and triphenylphosphine (114 mg, 0.44 mmol). The reaction mixture was stirred for 1 h and the solvent was removed under reduced pressure. The crude product was purified by flash chromatography on silica gel, eluting with diethyl ether/hexanes (5:95), to give chloride **27** (66.5 mg, 44%) as a white foam. $[\alpha]_D^{20} = -13.15$ (*c* 1.0, $CHCl_3$). ^{1}H NMR (300 MHz, $CDCl_3$) δ: 7.37–7.24 (m, 4H, 4×ArH), 7.13 (dd, *J* = 6.5 and 1.6 Hz,1H, ArH), 6.00 (s, 1H, H2), 4.56–4.49 (m, 1H, CHCl), 4.43 (m, 1H, H5), 4.00 (d, *J* = 3.3 Hz, 1H, H4), 3.20 (m, 2H, CH_2Ph), 2.30 (m, 2H, CH_2-6), 0.94 (s, 9H,C(CH_3)$_3$), 0.90 (s, 9H,C(CH_3)$_3$), 0.20 (s, 3H, CH_3), 0.14 (s, 3H, CH_3), 0.13 (s, 3H, CH_3) and 0.10 (s, 3H, CH_3) ppm. ^{13}C NMR (63 MHz, $CDCl_3$) δ: 175.2 (C), 137.9 (C), 136.8 (C), 135.3 (CH), 129.8 (2×CH), 127.3 (2×CH), 127.0 (CH), 75.7 (CH), 74.8 (C), 67.2 (CH), 61.0 (CH), 45.5 (CH_2), 37.0 (CH_2), 25.9 (C(*C*H_3)$_3$), 25.7 (C(*C*H_3)$_3$), 18.1 (*C*(CH_3)$_3$), 18.1 (*C*(CH_3)$_3$), –3.0 (2×CH_3), –4.1 (CH_3) and –4.4 (CH_3) ppm. IR (film): 1802 (CO) cm^{-1}. MS (ESI) *m/z* (%) 545 (MNa^+). HRMS calcd for $C_{27}H_{23}O_4ClNa$ (MNa^+): 545.2281; found, 545.2290.

(1*R*,4*R*,5*R*)-1,4-Dihydroxy-3-[(1*S*)-1-chloro-2-phenyl]ethylcyclohex-2-en-1,5-carbolactone (**28**). A stirred solution of the silylether **27** (66.5 mg, 0.13 mmol) in dry THF (3.0 mL), under argon at 0 ºC, was treated with tetrabutylammonium fluoride (0.3 mL, 0.3 mmol, *ca.* 1.0 M in THF). The mixture was stirred for 15 min, saturated NH_4Cl was added and the organic layer was extracted with diethyl ether (×3). The combined organic extracts were dried (anh. Na_2SO_4), filtered and concentrated under reduced pressure. The crude product was purified by flash chromatography on silica gel, eluting with (1:1:2) diethyl ether/acetone/hexanes, to give diol **28** (30 mg, 81%) as a white foam. $[\alpha]_D^{20} = -3.2$ (*c* 1.0, MeOH). ^{1}H NMR (250 MHz, CD_3OD) δ: 7.30–7.15 (m, 5H, 5xArH), 6.05 (s, 1H, H2), 4.79 (t, *J* = 6.8 Hz, 1H, CHCl), 4.57 (m, 1H, H5), 4.10 (d, *J* = 3.3 Hz, 1H, H4), 3.29 (dd, *J* = 13.8 and 6.6 Hz, 1H, C*H*HPh), 3.17 (dd, *J* = 13.8 and 7.3 Hz, 1H, CH*H*Ph) and 2.30 (m, 1H, CH_2-

6) ppm. ^{13}C NMR (63 MHz, CD_3OD) δ: 178.2 (C), 140.2 (C), 138.4 (C), 134.7 (CH), 130.8 (2×CH), 129.3 (2×CH), 127.8 (CH), 77.8 (CH), 74.1 (C), 66.6 (CH), 62.9 (CH), 45.6 (CH_2) and 37.2 (CH_2) ppm. IR (film): 3409 (OH) and 1777 (CO) cm^{-1}. MS (ESI) *m/z* (%) 317 (MNa^+). HRMS calcd for $C_{15}H_{15}O_4ClNa$ (MNa^+): 317.0551; found, 317.0543.

(1*R*,4*R*,5*R*)-1,4,5-Trihydroxy-3-[(1*S*)-1-chloro-2-phenyl]ethylcyclohex-2-en-1-carboxylic acid (9). A solution of carbolactone **28** (28 mg, 0.08 mmol) in THF (3.0 mL) at 0 ºC was treated with aqueous lithium hydroxide (0.10 mL, 0.10 mmol, 1 M) and the mixture was stirred for 2 h. Water was added and the THF was removed under reduced pressure. The resulting aqueous solution was washed with diethyl ether (×3) and the aqueous extract was treated with Amberlite IR-120 (H^+) until pH 6. The resin was filtered off and washed with Milli-Q water. The filtrate and the washings were lyophilized to give acid **9** (3.0 mg, 11%) as a white solid. $[\alpha]_D^{20}$ = –5.8 (*c* 1.0, MeOH). ^{1}H NMR (300 MHz, D_2O) δ: 7.41–7.36 (m, 5H, 5×ArH), 5.79 (s, 1H, H2), 4.59 (dd, *J* = 8.3 and 4.2 Hz, 1H, CHCl), 4.28 (d, *J* = 7.3 Hz, 1H, H4), 3.97 (q, *J* = 7.3 Hz, 1H, H5), 3.13 (dd, *J* = 13.6 and 4.2 Hz, 1H, C*H*HPh), 2.90 (dd, *J* = 13.6 and 8.3 Hz, 1H, CH*H*Ph) and 2.12 (d, *J* = 7.3 Hz, 2H, CH_2-6) ppm. ^{13}C NMR (63 MHz, D_2O) δ: 163.4 (C), 145.1 (C), 139.3 (C), 130.0 (2×CH), 129.2 (2×CH), 127.2 (CH), 125.1 (CH), 73.5 (C), 72.9 (CH), 72.8 (CH), 69.9 (CH), 41.9 (CH_2), and 38.8 (CH_2) ppm. IR (film): 3417 (OH) and 1640 (CO) cm^{-1}. MS (ESI) *m/z* (%) 311 (M–H). HRMS calcd for $C_{15}H_{17}O_5Cl$ (M–H): 311.1085; found, 311.1052.

Dehydroquinase assays. Both enzymes were purified as described previously.[35,36] Concentrated solutions of *Hp*-DHQ2 (6.4 mg mL^{-1}) or *Mt*-DHQ2 (2.4 mg mL^{-1}) were stored in potassium phosphate buffer (50 mM, pH 7.2), DTT (1 mM) and NaCl (150 mM). When required for assays, aliquots of the enzyme stock solutions were diluted in water and buffer and stored on ice. Dehydroquinase was assayed in the forward direction by monitoring the increase in absorbance at 234 nm in the UV spectrum due to the absorbance of the enone-carboxylate chromophore of 3-dehydroshikimic acid (**2**) (ε/M^{-1} cm^{-1} 12 000). Standard assay conditions were pH 7.0 at 25 ºC in Tris.HCl (50 mM) for *Hp*-DHQ2 and Tris.HOAc (50 mM) for *Mt*-DHQ2. Each assay was initiated by the addition of the substrate. Solutions of 3-dehydroquinic acid (**1**) were calibrated by equilibration

with DHQ2 and measurement of the change in the UV absorbance at 234 nm due to the formation of the enone-carboxylate chromophore of 3-dehydroshikimic acid (**2**). The K_i values of acids **5–10** against DHQ2 were obtained from Dixon plots (1/v *vs* [I]) of assay data. The initial rates at fixed enzyme and substrate concentrations (0.25–1.4 K_m) were measured in the absence and in the presence of various inhibitor concentrations.

Crystallization of *Mt*-DHQ2/5–8 binary complexes. Apo-*Mt*-DHQ2 crystals[37] were soaked in 10 mM solutions of inhibitors **5–8** in the crystallization mixture [32% (v/v) 2-methyl-2,4-pentanediol, 0.3 M ammonium sulfate and 0.1 M 4-(2-hydroxyethyl)-piperazine-1-ethanesulfonic acid sodium salt (HEPES sodium salt) pH 7.5] for 6 h (inhibitors **5**, **7** and **8**) and 20 h (inhibitor **6**).

Structure Determination of Binary Complexes. Crystals were harvested in reservoir solution supplemented with 20% (v/v) glycerol, mounted into cryoloops, and flash frozen by rapid immersion in liquid nitrogen. X-ray diffraction data for the *Mt*-DHQ2/**5** complex and *Mt*-DHQ2/**7–8** complexes were collected on beamlines ID23-2 and ID29 (ESRF, Grenoble, France), respectively, from crystals maintained at 100 K. Data for the *Mt*-DHQ2/**6** complex were collected on beamline BL13-Xaloc (Alba Synchrotron, Barcelona, Spain) from crystals maintained at 100 K. The data were processed, scaled, corrected for absorption effects and the crystal unit-cell parameters were calculated by global refinement using XDS,[38] SCALA,[39] and other programs from the CCP4 software suite.[40] The structures of *Mt*-DHQ2/**5**–**8** binary complexes were solved by molecular replacement using the program MOLREP[41] with a search model generated from PDB entry 1H0S.[28]

The structures and geometrical restraints of inhibitors were generated with the PRODRG2 server[42] and were manually placed during the model building, which was performed with COOT.[43] Reflections for calculating Rfree[44] were selected randomly and refinement of the models was performed with REFMAC[45] and final structure validation was performed with MOLPROBITY.[46] The data collection, refinement and model statistics are summarized in Table S1 of the Supporting Information. Figures depicting structures were prepared using PYMOL.[47]

Molecular dynamics simulations. *Ligand minimization*. Ligand geometries were optimized using a restricted

Hartree–Fock (RHF) method and a 6–31G(d,p) basis set, as implemented in the *ab initio* program Gaussian 09.[48] The charge distribution for each ligand studied was obtained by fitting the quantum mechanically calculated (B3LYP/cc-pVTZ and IEF-PCM as solvation model) molecular electrostatic potential (MEP) of the geometry-optimized molecule to a point charge model, as implemented in the assisted model building with energy refinement (AMBER)[49] suite of programs. The missing bonded and non-bonded parameters were assigned, by analogy or through interpolation from those already present in the AMBER database (GAFF).[50]

Generation and minimization of the DHQ2-ligand complexes. For *Mt*-DHQ2/**5**–**8** binary complexes, simulations were carried out using the enzyme geometries found in their respective crystal structures (PDB entries 4CIV, 4CIW, 4CIX and 4CIY, respectively). For *Mt*-DHQ2/**9**–**10** binary complexes, the enzyme geometries found in the crystal structures of *Mt*-DHQ2 in complex with ligands **7** (PDB entry 4CIX) and **8** (PDB entry 4CIY) were used after manual replacement of ligands **7**–**8** by **9**–**10**, respectively. Given that the minimum catalytic unit of DHQ2 was experimentally determined to be a trimer,[30] the latter was used for modelling. For *Mt*-DHQ2/**5** binary complex, unsolved residues were modelled using the web-based ModLoop server.[32] For *Mt*-DHQ2/**7**–**8** binary complexes, the missing residues were modelled as PDB entry 2XB8[15]. Hydrogens were added to the protein using the web-based PROPKA3.1 server,[51] which assigned protonation states to all titratable residues at the chosen pH of 7.0. However, δ and/or ε protonation was manually corrected for His102 (dual) of the active site due to mechanistic considerations and on the basis of results from preliminary MD simulations. Molecular mechanics parameters from the ff12SB and GAFF force fields, respectively, were assigned to the protein and the ligands using the LEaP module of AMBER 12.[52] All terminal hydrogens were first minimized in vacuum (2000 steps, half of them steepest descent, the other half conjugate gradient). Energy minimization was carried out in two stages using the implicit solvent GB model; firstly protein side chains (2000 steps, idem) and secondly the entire complex (1000 steps, idem). Thereafter, each molecular system was immersed in a truncated octahedron containing TIP3P[53] water molecules (10 Å radius) and Na^+ ions[54] to achieve electroneutrality.

Simulations. MD simulations were performed using the AMBER 11 suite of programs and Amber ff12SB force field. Periodic boundary conditions were applied and electrostatic interactions were treated using the smooth particle mesh Ewald method (PME)[55] with a grid spacing of 1 Å. The cutoff distance for the non-bonded

interactions was 9 Å. The SHAKE algorithm[56] was applied to all bonds containing hydrogen, using a tolerance of 10^{-5} Å and an integration step of 2.0 fs. Minimization was carried out in three steps, starting with the octahedron water hydrogens, followed by solvent molecules and sodium counterions and finally the entire system. The minimized system was heated at 300 K (1 atm, 25 ps, a positional *restraint* force constant of *50 kcal mol*$^{-1}$ Å^{-2}). These initial harmonic restraints were gradually reduced to *5 kcal mol*$^{-1}$ Å^{-2} (10 steps) and the resulting systems were allowed to equilibrate further. MD simulations were carried out for 10 ns. System coordinates were collected every 20 ps for further analysis.

ASSOCIATED CONTENT

Supporting Information

Extra figures for the reported crystal structures of *Mt*-DHQ2/**5–8** binary complexes, amino acid sequence alignments for DHQ2 enzymes from different sources and the MD simulation studies are included. Copies of ^{1}H NMR, ^{13}C NMR and DEPT spectra and Dixon plots for compounds **5**–**10** are also enclosed. This material is available free of charge via the Internet at http://pubs.acs.org.

Accession Codes

Coordinates and structure factors are available from the Protein Data Bank with accession codes 4CIV, 4CIW, 4CIX and 4CIY for *Mt*-DHQ2/**5**-**8** binary complexes, respectively.

AUTHOR INFORMATION

Corresponding Author

* E-mail: concepcion.gonzalez.bello@usc.es

Author Contributions

‡These authors contributed equally.

Notes

The authors declare no competing financial interest.

Funding Sources

Financial support from the Spanish Ministry of Science and Innovation (SAF2010-15076) and the Xunta de Galicia (GRC2013/041) is gratefully acknowledged. BB and AP thank the Spanish Ministry of Education for their respective FPU fellowships. AS thanks the Spanish Ministry of Economy and Competitiveness for her FPI fellowship. JMO thanks the Xunta de Galicia for a Plan I2C postdoctoral fellowship.

ACKNOWLEDGMENT

We thank ESRF beamlines ID23-2 and ID29 (Grenoble, France) and the ALBA synchrotron beamline BL13-XALOC (Barcelona, Spain) for the provision of beam time. We are also grateful to the Centro de Supercomputación de Galicia (CESGA) for use of the Finis Terrae computer.

ABBREVIATIONS USED

DHQ2, Type II Dehydroquinase; *Hp*-DHQ2, Type II Dehydroquinase from *Helicobacter pylori*; *Mt*-DHQ2, Type II Dehydroquinase from *Mycobacterium tuberculosis*; QM, quantum mechanics; MD, molecular dynamics; MM, molecular mechanics; WAT1, conserved water molecule; MM-PBSA, molecular mechanics Poisson–Boltzmann surface area.

REFERENCES

(1) Clatworthy, A. E.; Pierson, E.; Hung, D. T. Targeting virulence: a new paradigm for antimicrobial therapy. *Nat. Chem. Biol.* **2007**, *3*, 541–548.

(2) Mckenna, M. Antibiotic resistance: the last resort. *Nature* **2013**, *499*, 394–396.

(3) Fischbach, M. A.; Walsh, C. T. Antibiotics for emerging pathogens. *Science* **2009**, *325*, 1089–1093.

(4) Lewis, K. Platforms for antibiotic discovery. *Nat. Rev. Drug Discovery* **2013**, *12*, 371–387.

(5) Bush, K.; Courvalin, P.; Dantas, G.; Davies, J.; Eisenstein, B.; Huovinen, P.; Jacoby, G. A.; Kishony, R.; Kreiswirth, B. N.; Kutter, E.; Lerner, S. A.; Levy, S.; Lewis, K.; Lomovskaya, O.; Miller, J. H.; Mobashery, S.; Piddock, L. J. V.; Projan, S.; Thomas, C. M.; Tomasz, A.; Tulkens, P. M.; Walsh, T. R.; Watson, J. D.; Witkowski, J.; Witte, W.; Wright, G.; Yeh, P.; Zgurskaya, H. I. Tackling antibiotic resistance. *Nat. Rev. Microbiol.* **2011**, *9*, 894–896.

(6) Koul, A.; Arnoult, E.,; Lounis, N.; Guillemont, J.; Andries, K. The challenge of new drug discovery for tuberculosis. *Nature* **2011**, *469*, 483–490.

(7) Butler, D. New fronts in an old war. *Nature* **2000**, *406*, 670–672.

(8) Walsh, C. Antibiotics: actions, origins, resistance. ASM Press: Washington, D. C., 2003.

(9) Lamichhane, G.; Freundlich, J. S.; Ekins, S.; Wickramaratne, N.; Nolan, S. T.; Bisha, W. R. Essential metabolites of *Mycobacterium tuberculosis* and their mimics. *mBio* **2011**, *2*, e00301–e00310.

(10) Data base for essential genes in bacteria see www.essentialgene.org.

(11) Krell, T.; Pitt, A. R.; Coggins, J. R. The use of electrospray mass spectrometry to identify an essential arginine residue in type II dehydroquinases. *FEBS Lett.* **1995**, *360*, 93–96.

(12) Krell, T.; Horsburgh, M. J.; Cooper, A.; Kelly, S. M.; Coggins, J. R. Localization of the active site of type II dehydroquinase. Identification of a common arginine-containing motif in the two classes of dehydroquinases. *J. Biol. Chem.* **1996**, *271*, 24492–24497.

(13) Coderch, C.; Lence, E.; Peón, A.; Lamb, H.; Hawkins, A. R.; Gago, F.; González-Bello, C. Mechanistic insight into the reaction catalyzed by bacterial type II dehydroquinases. *Biochem. J.* **2014**, *458*, 547–557.

(14) Harris, J.; González-Bello, C.; Kleanthous, C.; Coggins, J. R.; Hawkins, A. R.; Abell, C. Evidence from kinetic isotope studies for an enolate intermediate in the mechanism of type II dehydroquinases. *Biochem. J.* **1996**, *319*, 333–336.

(15) Peón, A.; Otero, J. M.; Tizón, L.; Prazeres, V. F. V.; Llamas-Saiz, A. L.; Fox, G. C.; van Raaij, M. J.; Lamb, H.; Hawkins, A. R.; Gago F.; Castedo, L.; González-Bello, C. Understanding the key factors that control the inhibition of type II dehydroquinase by (2*R*)-2-benzyl-3-dehydroquinic acids. *ChemMedChem* **2010**, *5*, 1726–1733.

(16) Roszak, A. W.; Robinson, D. A.; Krell, T.; Hunter, I. S.; Frederickson, M.; Abell, C.; Coggins, J. R.; Lapthorn, A. J. The structure and mechanism of the type II dehydroquinase from *Streptomyces coelicolor*. *Structure* **2002**, *10*, 493–503.

(17) Blomberg, L. M.; Mangold, M.; Mitchell, J. B. O.; Blumberger, J. Theoretical study of the reaction mechanism of *Streptomyces coelicolor* type II dehydroquinase. *J. Chem. Theory Comput.* **2009**, *5*, 1284–1294.

(18) Tizón, L.; Otero, J. M.; Prazeres, V. F. V.; Llamas-Saíz, A. L.; van Raaij, M. J.; Lamb, H.; Hawkins, A. R.; Ainsa, J. A.; Castedo, L.; González-Bello, C. A prodrug approach for improving anti-tuberculosis activity of potent *Mycobacterium tuberculosis* type II dehydroquinase inhibitors. *J. Med. Chem.* **2011**, *54*, 6063–6084.

(19) Blanco, B.; Sedes, A.; Peón, A.; Lamb, H.; Hawkins, A. R.; Castedo, L.; González-Bello, C. Synthesis of 3-alkyl enol mimics inhibitors of type II dehydroquinase: factors influencing their inhibition potency. *Org. Biomol. Chem.* **2012**, *10*, 3662–3676.

(20) Prazeres, V. F. V.; Tizón, L.; Otero, J. M.; Guardado-Calvo, P.; Llamas-Saiz, A. L.; van Raaij, M. J.; Castedo, L.; Lamb, H.; Hawkins, A. R.; González-Bello, C. Synthesis and biological evaluation of new nanomolar competitive inhibitors of *Helicobacter pylori* type II dehydroquinase. Structural details of the role of the aromatic moieties with essential residues. *J. Med. Chem.* **2010**, *53*, 191–200.

(21) Babine, R. E.; Blender, S. L. Molecular recognition of protein−ligand complexes: applications to drug design. *Chem. Rev.* **1997**, *97*, 1359–1469.

(22) Lam, P. Y.; Jadhav, P. K.; Eyermann, C. J.; Hodge, C. N.; Ru, Y.; Bacheler, L.T.; Meek, J. L.; Otto, M. J.; Rayner, M. M.; Wong, Y. N.; Chang, C.-H.; Weber, P.; Jackson, D.A.; Sharpe, T. R.; Erickson-Viitanen, S. Rational design of potent, bioavailable, nonpeptide cyclic ureas as HIV protease inhibitors. *Science* **1994**, *263*, 380–384.

(23) Romines, K. R.; Watenpaugh, K. D.; Howe, W. J.; Tomich, P. K.; Lovasz, K. D.; Morris, J. K.; Janakiraman, M. N.; Lynn, J. C.; Horng, M.-M.; Chong, K.-T.; Hinshaw, R. R.; Dolak, L. A. Structure-

based design of nonpeptidic HIV protease inhibitors from a cyclooctylpyranone lead structure. *J. Med. Chem.* **1995**, *38*, 4463–4473.

(24) Vara Prasad, J. V. N.; Lunney, E. A.; Ferguson, D.; Tummino, P. J.; Rubin, J. R.; Reyner, E. L.; Stewart, B. H.; Guttendorf, R. J.; Domagala, J. M.; Suvorov, L. I.; Gulnik, S. V.; Topol, I. A.; Bhat, T. N.; Erickson, J. W. HIV protease inhibitors possessing a novel, high-affinity, and achiral P1'/P2/ligand with a unique pattern of *in vitro* resistance. Importance of a conformationally-restricted template in the design of enzyme inhibitors. *J. Am. Chem. Soc.* **1995**, *117*, 11070–11074.

(25) Montchamp, J.-L.; Frost, J. W. Cyclohexenyl and cyclohexylidene inhibitors of 3-dehydroquinate synthase: active site interactions relevant to enzyme mechanism and inhibitor design. *J. Am. Chem. Soc.* **1997**, *119*, 7645–7653.

(26) Sánchez-Sixto, C.; Prazeres, V. F. V.; Castedo, L.; Lamb, H.; Hawkins, A. R.; González-Bello, C. Structure-based design, synthesis and biological evaluation of inhibitors of *Mycobacterium tuberculosis* type II dehydroquinase. *J. Med. Chem.* **2005**, *48*, 4871–4881.

(27) Peón, A.; Coderch, C.; Gago, F.; González-Bello, C. Comparative binding energy (COMBINE) analysis for understanding the binding determinants of type II dehydroquinase inhibitors. *ChemMedChem* **2013**, *8*, 740–747.

(28) The X-ray crystal structure is available from the Protein Data Bank (PBD code: 1H0S): Robinson, D. A.; Roszak, A. W.; Frederickson, M.; Abell, C.; Coggins, J. R.; Lapthorn, A. J. Structural basis for specificity of oxime based inhibitors towards type II dehydroquinase from *M. tuberculosis*. Unpublished material.

(29) For *Mt*-DHQ2/**5** (PDB entry 4CIV): rms differences of 0.249 Å and 0.225 Å after superposition of 125 and 126 C^{α}-atom pairs of PDB 2XB8 and 2Y71, respectively. For *Mt*-DHQ2/**6** (PDB entry 4CIW): rms differences of 0.161 Å and 0.120 Å after superposition of 118 and 115 C^{α}-atom pairs of PDB 2XB8 and 2Y71, respectively.

(30) Price, N. C.; Boam, D. J.; Kelly, S. M.; Duncan, D.; Krell, T.; Gourley, D. G.; Coggins, J. R.; Virden, V.; Hawkins, A. R. The folding and assembly of the dodecameric type II dehydroquinases. *Biochem. J.* **1999**, *338*, 195–202.

(31) Cornell, W. D.; Cieplak, P.; Bayly, C. I.; Gould, I. R.; Merz, K. M.; Ferguson, D. M.; Spellmeyer, D. C.; Fox, T.; Caldwell, J. W.; Kollman, P. A. A second generation force field for the simulation of proteins, nucleic acids, and organic molecules. *J. Am. Chem. Soc.* **1995**, *117*, 5179−5197.

(32) Fiser, A.; Sali, A. ModLoop: automated modeling of loops in protein structures. *Bioinformatics* **2003**, *19*, 2500–2501.

(33) Bissantz, C.; Kuhn, B.; Stahl, M. A medicinal chemist´s guide to molecular interactions. *J. Med. Chem.* **2010**, *53*, 5061−5084.

(34) Miller III, B. R.; McGee Jr., T. D.; Swails, J. M.; Homeyer, N.; Gohlke, H.; Roitberg, A. E. MMPBSA.py: an efficient program for end-state free energy calculations. *J. Chem. Theory Comput.* **2012**, *8*, 3314−3321.

(35) Prazeres, V. F. V.; Sánchez-Sixto, C.; Castedo, L.; Shuh, S. W.; Lamb, H.; Hawkins, A. R.; Cañada, F. J.; Jiménez-Barbero, J.; González-Bello, C. Competitive inhibitors of *Helicobacter pylori* type II dehydroquinase: synthesis, biological evaluation, and NMR studies. *ChemMedChem* **2008**, *3*, 756–770.

(36) Gourley, D. G.; Coggins, J. R.; Isaacs, N. W.; Moore, J. D.; Charles, I. G.; Hawkins, A. R. Crystallization of a type II dehydroquinase from *Mycobacterium tuberculosis*. *J. Mol. Biol.* **1994**, *241*, 488–491.

(37) Gourley, D. G.; Shrive, A. K.; Polikarpov, I.; Krell, T.; Coggins, J. R.; Hawkins, A. R.; Isaacs, N. W.; Sawyer, L. The two types of 3-dehydroquinase have distinct structures but catalyse the same overall reaction. *Nat. Struct. Biol.* **1999**, *6*, 521−525.

(38) Kabsch, W. *XDS. Acta Cryst.* **2010**, *D66*, 125−132.

(39) Evans, P. Scaling and assessment of data quality. *Acta Cryst.* **2006**, *D62*, 72–82.

(40) Winn, M. D. An overview of the CCP4 project in protein crystallography: an example of a collaborative project. *J. Synchrotron Radiat.* **2003**, *10*, 23–25.

(41) Vagin, A.; Teplyakov, A. MOLREP: an automated program for molecular replacement. *J. Appl. Cryst.* **1997**, *30*, 1022–1025.

(42) Schüttelkopf, A. W.; van Aalten, D. M. F. PRODRG: a tool for high-throughput crystallography of protein-ligand complexes. *Acta Cryst.* **2004**, *D60*, 1355−1363.

(43) Emsley, P.; Cowtan, K. Coot: model-building tools for molecular graphics. *Acta Cryst.* **2004**, *D60*, 2126−2132.

(44) Brünger, A. T. Free R value: cross-validation in crystallography. *Methods Enzymol.* **1997**, *277*, 366−396.

(45) Murshudov, G. N.; Vagin, A. A.; Dodson, E. J. Refinement of macromolecular structures by the maximum-likelihood method. *Acta Cryst.* **1997**, *D53*, 240−255.

(46) Davis, I. W.; Leaver-Fay, A.; Chen, V. B.; Block, J. N.; Kapral, G. J.; Wang, X.; Murray, L. W.; Arendall, W. B. 3rd; Snoeyink, J.; Richardson, J. S.; Richardson, D. C. MolProbity: all-atom contacts and structure validation for proteins and nucleic acids. *Nucleic Acids Res.* **2007**, *35*, W375−W383.

(47) DeLano, W. L. The PyMOL molecular graphics system. (2008) DeLano Scientific LLC, Palo Alto, CA, USA. http://www.pymol.org

(48) Gaussian 09, revision A.2: Frisch, M. J.; Trucks, G. W.; Schlegel, H. B.; Scuseria, G. E.; Robb, M. A.; Cheeseman, J. R.; Scalmani, G.; Barone, V.; Mennucci, B.; Petersson, G. A.; Nakatsuji, H.; Caricato, M.; Li, X.; Hratchian, H. P.; Izmaylov, A. F.; Bloino, J.; Zheng, G.; Sonnenberg, J. L.; Hada, M.; Ehara, M.; Toyota, K.; Fukuda, R.; Hasegawa, J.; Ishida, M.; Nakajima, T.; Honda, Y.; Kitao, O.; Nakai, H.; Vreven, T.; Montgomery, Jr. J. A.; Peralta, J. E.; Ogliaro, F.; Bearpark, M.; Heyd, J. J.; Brothers, E.; Kudin, K. N.; Staroverov, V. N.; Kobayashi, R.; Normand, J.; Raghavachari, K.; Rendell, A.; Burant, J. C.; Iyengar, S. S.; Tomasi, J.; Cossi, M.; Rega, N.; Millam, J. M.; Klene, M.; Knox, J. E.; Cross, J. B.; Bakken, V.; Adamo, C.; Jaramillo, J.; Gomperts, R.; Stratmann, R. E.; Yazyev, O.; Austin, A. J.; Cammi, R.; Pomelli, C.; Ochterski, J. W.; Martin, R. L.; Morokuma, K.; Zakrzewski, V. G.; Voth, G. A.; Salvador, P.; Dannenberg, J. J.; Dapprich, S.; Daniels, A. D.; Farkas, Ö.; Foresman, J. B.; Ortiz, J. V.; Cioslowski, J.; Fox, D. J. Gaussian, Inc., Wallingford CT, **2009**.

(49) Case, D. A.; Cheatham, T. E.; Darden, T.; Gohlke, H., Luo, R.; Merz, K. M.; Onufriev, O.; Simmerling, C.; Wang, B.; Woods, R. J. The AMBER biomolecular simulation program. *J. Comput. Chem.* **2005**, *26*, 1668–1688.

(50) Wang, J.; Wang, W.; Kollman, P. A.; Case, D. A. Automatic atom type and bond type perception in molecular mechanical calculations. *J. Mol. Graphics Modell.* **2006**, *25*, 247–260.

(51) Olsson, M. H. M.; Søndergard, C. R.; Rostkowski, M.; Jensen, J. H. PROPKA3: consistent treatment of internal and surface residues in empirical pK_a predictions, *J. Chem. Theory Comput.* **2011**, *7*, 525–537.

(52) AMBER tools 13 and AMBER 12: Case, D. A.; Darden, T. A.; Cheatham III, T. E.; Simmerling, C. L.; Wang, J.; Duke, R. E.; Luo, R.; Walker, R. C.; Zhang, W.; Merz, K. M.; Roberts, B.; Hayik, S.; Roitberg, A.; Seabra, G.; Swails, J.; Goetz, A. W.; Kolossváry, I.; Wong, K. F.; Paesani, F.; Vanicek, J.; Wolf, R. M.; Liu, J.; Wu, X.; Brozell, S. R.; Steinbrecher, T.; Gohlke, H.; Cai, Q.; Ye, X.; Wang, J.; Hsieh, M.-J.; Cui, G.; Roe, D. R.; Mathews, D. H.; Seetin, M. G.; Salomon-Ferrer, R.; Sagui, C.; Babin, V.; Luchko, T.; Gusarov, S.; Kovalenko, A.; and Kollman, P. A. AMBER 12, University of California, San Francisco, **2012**.

(53) Jorgensen, W. L.; Chandrasekhar, J.; Madura, J. D. Temperature and size dependence for Monte Carlo simulations of TIP4P water. *J. Chem. Phys.* **1983**, *79*, 926–935.

(54) Aqvist, J. Ion-water interaction potentials derived from free energy perturbation simulations. *J. Phys. Chem.* **1990**, *94*, 8021–8024.

(55) Darden, T. A.; York, D.; Pedersen, L. G. Particle mesh Ewald: An W log(N) method for Ewald sums in large systems. *J. Chem. Phys.* **1993**, *98*, 10089–10092.

(56) Ryckaert, J.-P.; Ciccotti, G.; Berendsen, H. J. C. Numerical integration of the cartesian equations of motion of a system with constraints: molecular dynamics of n-alkanes. *J. Comput. Phys.* **1977**, *23*, 327–341.

Scheme 1. Reaction Mechanism for the Enzymatic Conversion of 3-Dehydroquinic Acid (1) to 3-Dehydroshikimic Acid (2) Catalyzed by the DHQ2 Enzyme.[a]

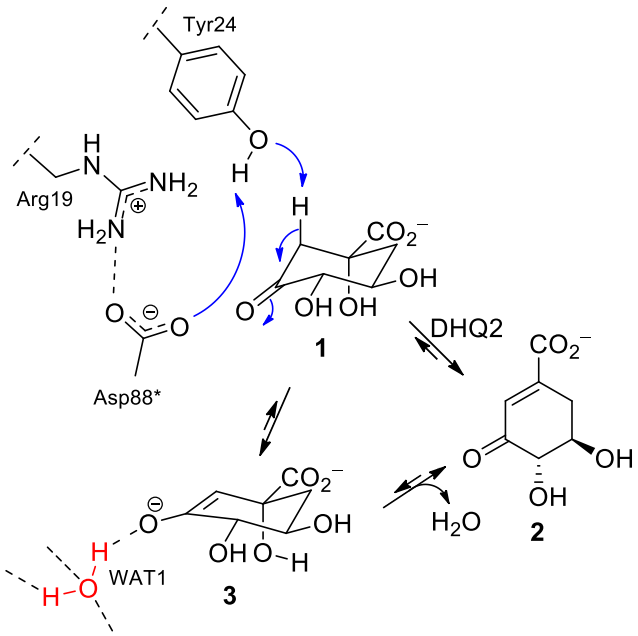

[a] The reaction proceeds *via* enolate intermediate **3**. Relevant residues are indicated. For the *Hp*-DHQ2 enzyme, the generation of the catalytic tyrosinate takes place with the assistance of a water molecule (not shown), while for *Mt*-DHQ2, the tyrosine is directly deprotonated by the aspartate residue.

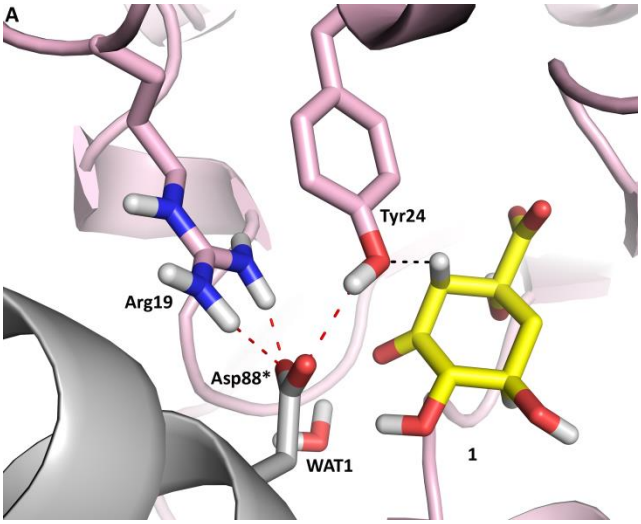

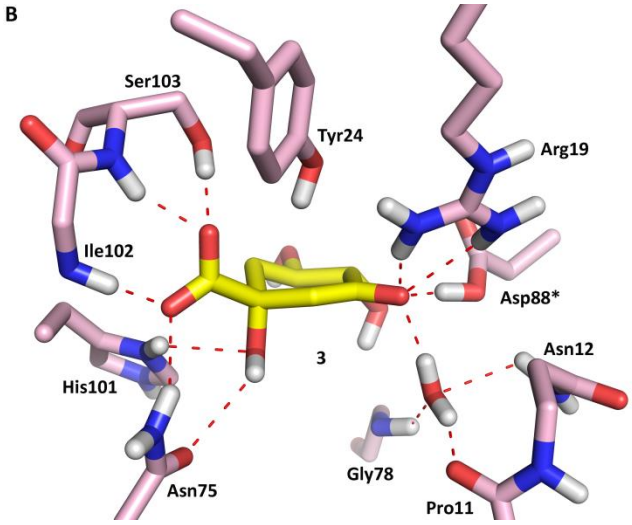

Figure 1. View of the *Mt*-DHQ2 Michaelis complex (A) and enolate intermediate **3** geometries (B) obtained by MD and QM/MM studies. Note how Asp88* from a neighboring enzyme subunit is responsible for the generation of the catalytic form of the essential tyrosine (tyrosinate) and that the enolate intermediate **3** is stabilized by the guanidinium group of Arg19 and hydrogen bonding with WAT1 and the neutral Asp88*. Relevant residues and water molecules are indicated and labeled. Hydrogen bonds (red) and key distances (black) are shown.

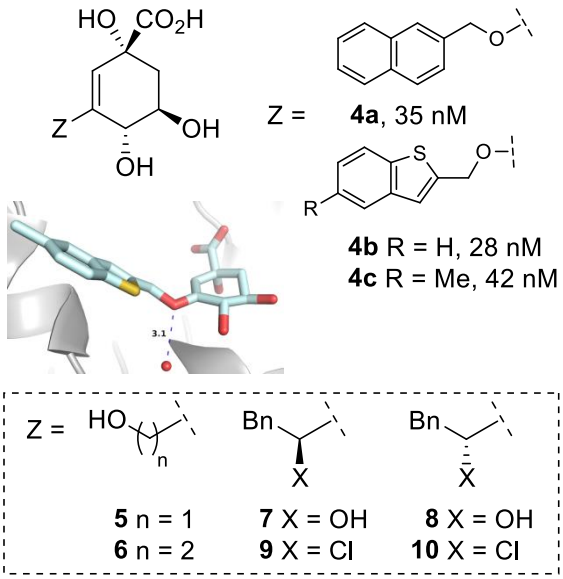

Figure 2. Selected examples of 3-methoxyaryl derivatives **4** that are DHQ2 competitive inhibitors and new target compounds **5**–**10**. A selected view of the crystal structure of the *Mt*-DHQ2/**4c** binary complex (PDB: 2Y71, 1.5 Å) is shown along with the K_i values of **4** against *Mt*-DHQ2.

Scheme 2. **Synthesis of Compounds 5 and 6**.[a]

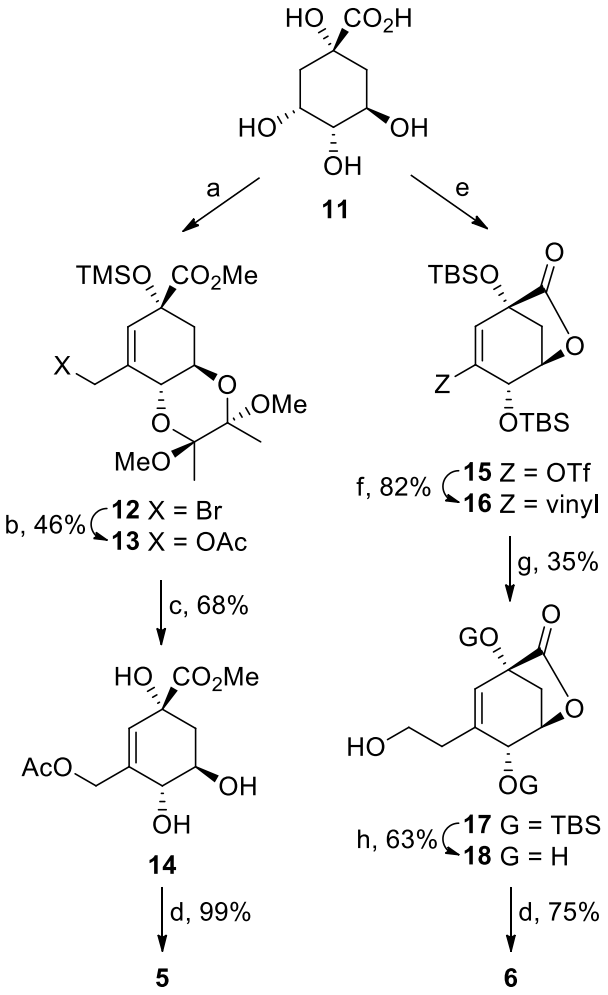

[a]*Reagents and conditions*: (a) ref. 20. (b) NaOAc, DMF, RT. (c) TFA/H_2O (20:1), 0 ºC. (d) 1. LiOH (aq.), THF, RT. 2. Amberlite IR-120 (H^+), RT. (e) ref. 21. (f) vinyl boronic acid pinacol ester, $Pd(PPh_3)_4$, K_2CO_3 (aq), dioxane, Δ. (g) 1. BH_3-THF, 0 ºC; 2. $NaBO_3$ (aq). (h) TBAF, THF, RT.

Scheme 3. **Synthesis of Compounds 7–10**.[a]

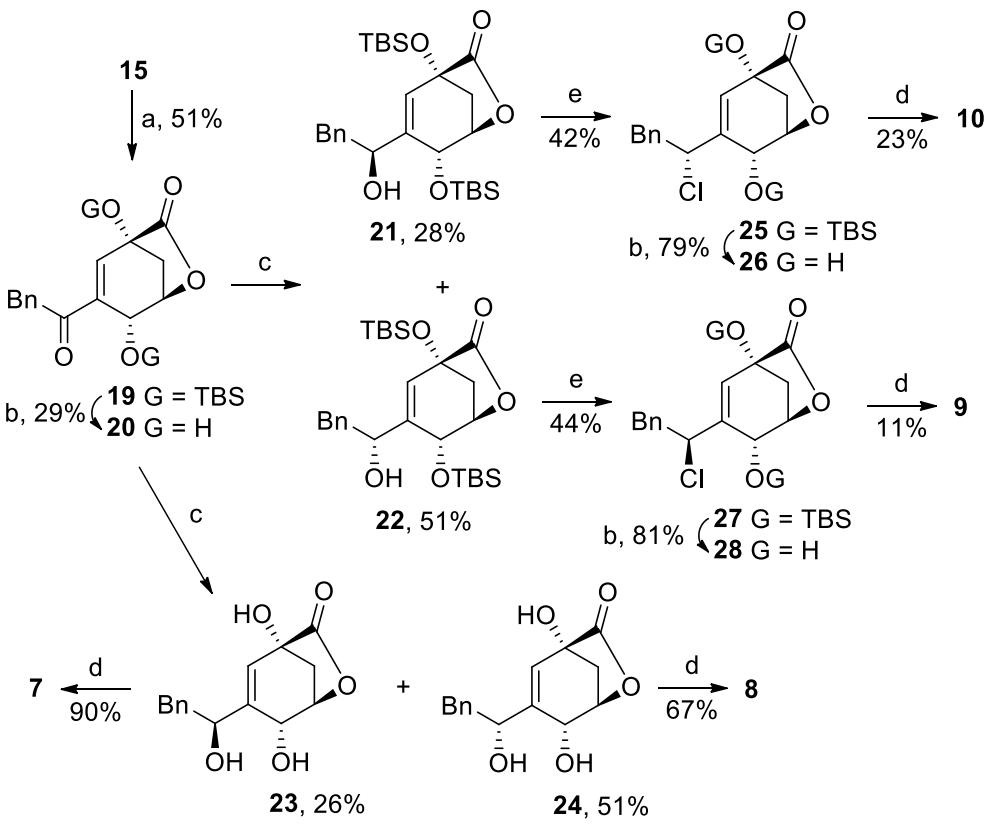

[a]*Reagents and conditions*: (a) CO, B-benzyl-9-BBN, $Pd(dppf)Cl_2$ (cat), K_3PO_4 (aq.), THF, 55 ºC. (b) TBAF, THF, RT. (c) $NaBH(OAc)_3$, $CeCl_3$, MeOH, THF, 0 ºC. (d) 1. LiOH (aq.), THF, RT. 2. Amberlite IR-120 (H^+), RT. (e) NCS, PPh_3, THF, RT.

Table 1. K_i (µM) values forcompounds 5–10 against *Hp*- and *Mt*-DHQ2 enzymes

Entry	Compound	Z	*Hp*-DHQ2[a]	*Mt*-DHQ2[b]
1	**5**		282 ± 8	11.2 ± 0.2
2	**6**	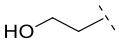	188 ± 4	15.0 ± 0.5
3	**7**		37.0 ± 0.2	34.0 ± 0.4
4	**8**		33.0 ± 0.3	27.0 ± 0.5
5	**9**		40.5 ± 4.6	14.5 ± 0.2
6	**10**		10.5 ± 0.2	0.48 ± 0.02

[a]Assay conditions: pH 7.0, 25 ºC, 50 mM Tris.HCl; K_m (**1**) = 444 µM;. [b]Assay conditions: pH 7.0, 25 ºC, 50 mM Tris.HOAc; K_m (**1**) = 15 µM.

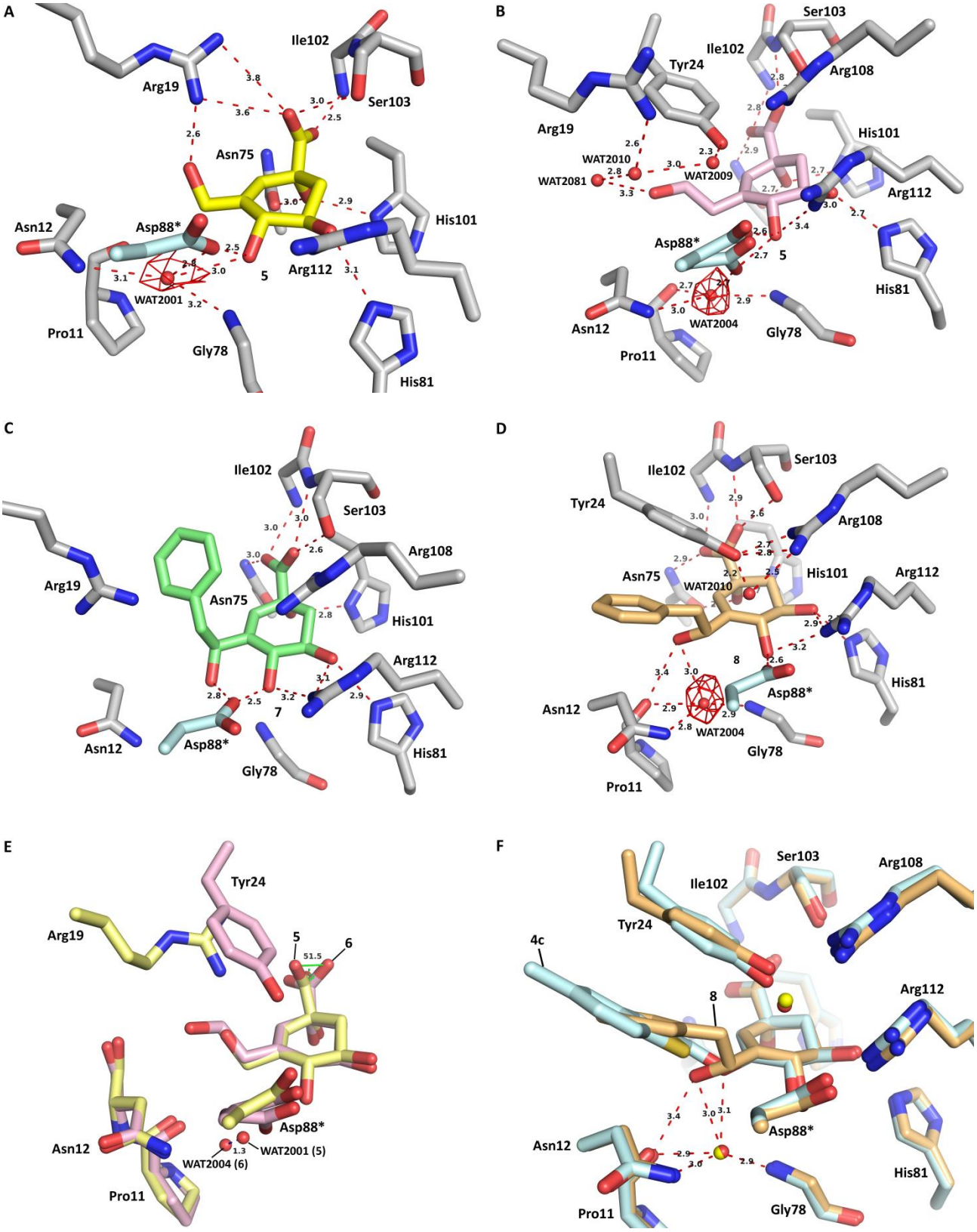

Figure 3. Binding interactions of inhibitors **5** (yellow), **6** (pink), **7** (green) and **8** (orange) in the binary complexes *Mt*-DHQ2/**5** (a, PDB entry 4CIV), *Mt*-DHQ2/**6** (b, PDB entry 4CIW), *Mt*-DHQ2/**7** (c, PDB entry 4CIX) and *Mt*-DHQ2/**8** (d, PDB entry 4CIY). Comparison of the binary complexes *Mt*-DHQ2/**5** (yellow) *vs* *Mt*-DHQ2/**6** (pink) and *Mt*-DHQ2/**8** (orange) *vs* *Mt*-DHQ2/**4c** (PDB entry 2Y71, cyan) are also shown in e) and f),

respectively. A maximum-likelihood weighted $2F_o - F_c$ map contoured at 1σ is shown up to 1.6 Å around the WAT1 molecule (red). For better comparison, water molecules in PDB entry 2Y71 are shown in yellow. Hydrogen-bonding interactions and distance differences between WAT2004 and WAT2001 are shown as red and blue dashes, respectively. Relevant residues are shown and labeled. For a)–d), the Asp88* residue from a symmetry-related neighboring enzyme subunit is shown in cyan.

Table 2. Crystallographic Data Collection and Refinement Statistics for the *Mt*-DHQ2 Complexes with Inhibitors 5–8

data processing[a]	*Mt*-DHQ2/**5**	*Mt*-DHQ2/**6**	*Mt*-DHQ2/**7**	*Mt*-DHQ2/**8**
space group	*F*23	*F*23	*F*23	*F*23
cell parameters (*a*, *b*, *c*), Å	126.18	126.38	126.36	126.21
wavelength (Å)	0.87260	1.00614	0.97908	0.97908
detector	MarMOSAIC 225	PILATUS 6M	PILATUS 6M	PILATUS 6M
observed reflections[b]	17629 (846)[c]	36731 (3129)[c]	17936 (2708)[c]	56471 (8655)[c]
resolution range (Å)	38.00 – 2.90 (3.06 – 2.90)	38.11 – 2.20 (2.32 – 2.20)	44.67 – 2.90 (3.06 – 2.90)	44.62 – 2.10 (2.21 – 2.10)
Wilson B ($Å^2$)	37.2	17.7	25.6	25.6
multiplicity	5.7 (2.2)	4.3 (2.6)	4.8 (5.1)	5.7 (5.9)
completeness	0.818 (0.710)	0.992 (0.954)	0.993 (1.000)	0.999 (1.000)
R_{merge}	0.082 (0.374)	0.089 (0.253)	0.113 (0.348)	0.062 (0.391)
Refinement[d]				
resolution range (Å)	36.45 – 2.90 (3.06 – 2.90)	38.13 – 2.20 (2.32 – 2.20)	38.13 – 2.90 (3.06 – 2.90)	38.08 – 2.10 (2.21 – 2.10)
reflections used in refinement[c]	2958 (355)	8152 (1122)	3589 (504)	9359 (1359)
reflections used for R_{free}	141 (26)	409 (72)	168 (31)	472 (70)
R-factor[e]	0.212 (0.299)	0.142 (0.181)	0.152 (0.222)	0.145 (0.166)
R_{free}[f]	0.279 (0.405)	0.192 (0.296)	0.189 (0.269)	0.197 (0.224)
rmsd (bonds (Å)/angles (°))	0.005/1.1	0.013/1.5	0.009/1.3	0.017/1.8
Final model				
protein/inhibitor/water/sodium/sulfate/chloride atoms	1038/14/22/0/0/0	1089/15/81/3/5/0	1006/21/6/0/10/0	1053/21/92/3/5/1
average B protein/inhibitor/water/sodium/sulfate/chloride ($Å^2$)	38.3/53.1/16.4/0/0/0	23.3/26.3/30.0/40.1/53.3/0	27.9/37.2/18.6/0/69.3/0	31.9/42.1/37.4/46.0/78.2/32.2
Ramachandran statistics[g] (%)	95.5/99.3	99.3/100.0	96.1/100.0	96.2/100.0

PDB accession code	4CIV	4CIW	4CIX	4CIY

[a]Results from SCALA.[39] [b]No sigma cut-off or other restrictions were used for inclusion of reflections. [c]Values in parentheses are for the highest resolution bin, where applicable. [d]Results from REFMAC.[45] [e]*R*-factor = $\sum ||Fobs(hkl)| |Fcalc(hkl)|| / \sum |Fobs(hkl)|$. [f]According to Brünger.[44] [g]According to the program MOLPROBITY.[46] The percentages indicated are for residues in favored and total allowed regions, respectively.

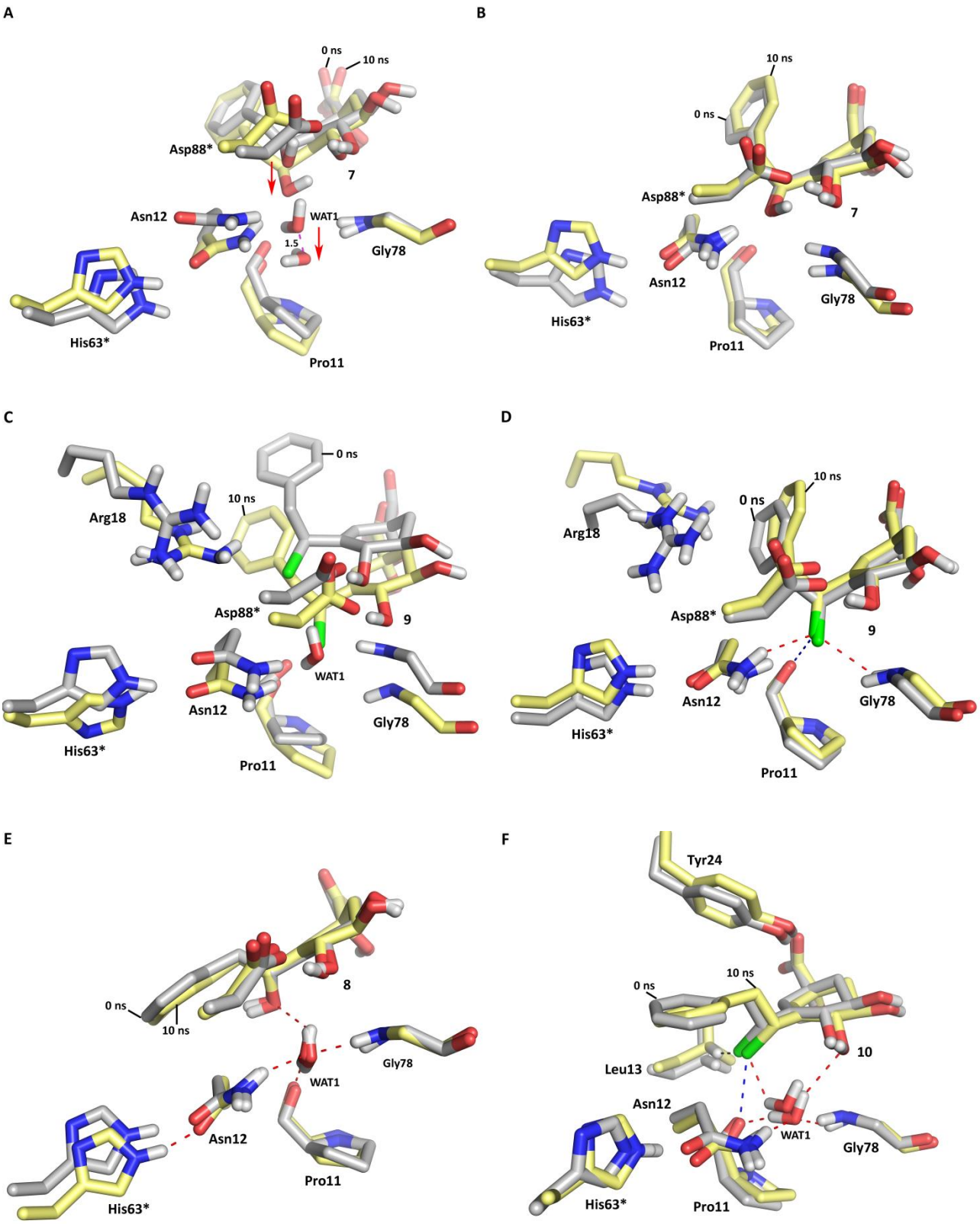

Figure 4. Comparison of the binding mode of the inhibitors **7**, **8**, **9** and **10** in the binary complexes *Mt*-DHQ2/**7** (A,B), *Mt*-DHQ2/**8** (E), *Mt*-DHQ2/**9** (C,D) and *Mt*-DHQ2/**10** (F) after minimization and prior simulation (gray) and after 10 ns of dynamic simulation (yellow). For *Mt*-DHQ2/**7** and *Mt*-DHQ2/**9** binary complexes, MD simulations were carried out with (A,C) and without WAT1 (B,D), respectively. Note how, for the *Mt*-DHQ2/**9**

binary complex, WAT1 is expelled from the WAT1 binding pocket during simulation while remains in place for *Mt*-DHQ2/**10**. Relevant side chain residues are shown and labeled. Relevant hydrogen-bonding (red), halogen-bonding (blue) and CH…Cl interactions (black) are shown. For *Mt*-DHQ2/**7** binary complex (A), distance differences between WAT1 after minimization and prior simulation and after 10 ns of dynamic simulation are shown as dashed lines (magenta).

TOC GRAPHIC